

12



DTIC
S ELECTIC D
MAR 27 1987
D

Progress Report

Investigation of the Icosahedral Z-Phase
in Aluminum Transition Metal Alloys
and Rapidly Solidified Al-Alloys

L. Bendersky, D. Shechtman and E. Horowitz

The Johns Hopkins University
G.W.C. Whiting School of Engineering
Materials Science and Engineering Department
Baltimore, Maryland 21218

Attn: E. Horowitz: (301) 338-7916

AD-A178 451

DTIC FILE COPY

DARPA Order No. 5527 (5-30-85)
ONR Order No. N00014-85-K-0779
Effective Date: 08-01-85
Expiration Date 06-30-87
Sponsored By: Defense Advanced Research Projects Agency
(DARPA)
and The Office of Naval Research (ONR)

September 1986

DISTRIBUTION STATEMENT A
Approved for public release
Distribution Unlimited

87. 3 12 106

Progress Report

Investigation of the Icosahedral Z-Phase
in Aluminum Transition Metal Alloys
and Rapidly Solidified Al-Alloys

L. Bendersky, D. Shechtman and E. Horowitz

The Johns Hopkins University
G.W.C. Whiting School of Engineering
Materials Science and Engineering Department
Baltimore, Maryland 21218

Attn: E. Horowitz: (301) 338-7916

DARPA Order No. 5527 (5-30-85)
ONR Order No. N00014-85-K-0779
Effective Date: 08-01-85
Expiration Date 06-30-87
Sponsored By: Defense Advanced Research Projects Agency
(DARPA)
and The Office of Naval Research (ONR)

September 1986



Accession For	
NTIS CRA&I	<input checked="" type="checkbox"/>
DTIC TAB	<input type="checkbox"/>
Unannounced	<input type="checkbox"/>
Justification	
By <i>lta on file</i>	
Distribution/	
Availability Codes	
Dist	Avail and/or Special
A-1	

Table of Contents

Executive Summary

1. Replacement of Icosahedral Al-Mn by Decagonal Phase.
R.J. Schaefer and L. Bendersky
Scripta Met., 20, 745-50 (1986)
2. Determination of The Point Group of The Icosahedral Phase in Al-Mn-Si Alloy using Convergent-Beam Electron Diffraction.
L.A. Bendersky and M.J. Kaufman
Phil. Mag. B., 53, L75-80 (1986)
3. Nucleation Behavior of Al-Mn Icosahedral Phase.
L.A. Bendersky and S.D. Ridder
J. Mater. Res. 1(3), 405-13 (May/June 1986)
4. An Analysis of the Microstructure of Rapidly Solidified Al-8 Wt. Pct. Fe Powder.
W.J. Boettinger, L. Bendersky and J.G. Early
Met. Trans. A., 17A, 781-90 (May 1986)
5. Rapidly Solidified Al-Cr Alloys: Structure and Decomposition Behavior.
L. Bendersky, R.J. Schaefer, F.S. Biancaniello and D. Shechtman
J. Mater. Sci., 21, 1989-96 (1986)

Executive Summary

The discovery by Shechtman, et. al. ^{1,2} of five-fold symmetry in rapidly solidified aluminum alloys stimulated world wide interest and activity in the preparation and properties of these materials. Likewise, research on the microstructure of a variety of rapidly solidified aluminum alloys including those containing ^{Iron} Fe and ^{Chromium} Cr has been advanced. This report covers the work of two Principal Investigators, Dr. Leo Bendersky and Dr. Dan Shechtman, plus their research collaborators, which has been reported in the scientific literature during the first half of 1986.

The five publications reproduced here represent a significant contribution to our understanding of the icosahedral phase and the microstructure of rapidly solidified alloys.

1. Shechtman, D. and Blech, I., Met. Trans. 16A, 1005 (1985).
2. Shechtman, D., Blech, I., Gratias, D. and Cahn, J.W., Phy. Rev. Lett., 53, 1951 (1984).

①

REPLACEMENT OF ICOSAHEDRAL Al-Mn BY DECAGONAL PHASE

R. J. Schaefer* and L. Bendersky**

* Metallurgy Division, National Bureau of Standards, Gaithersburg, MD 20899

** Center for Materials Research, The Johns Hopkins University, Baltimore, MD 21218

(Received February 3, 1986)

Introduction

Rapidly solidified alloys of Al containing 15-40 wt% Mn contain the icosahedral (1,2) and the decagonal (also called "T") (3) quasicrystal phases, both showing sharp diffraction with noncrystallographic point groups $m\bar{3}5$ and $10/m$ (or $10/mmm$) respectively. The unusual symmetries of these structures both require quasi-periodic lattice structures, although the decagonal phase is periodic along its ten-fold axis. While the icosahedral phase has received intensive theoretical and experimental study, the decagonal phase has attracted less attention and is usually regarded as an impediment to the formation of icosahedral material. However, the decagonal phase provides an important link between periodic and quasiperiodic structures, and its solidification behavior often sets the limits on the conditions under which the icosahedral phase forms. In this paper, we show that the decagonal phase is nucleated by and then replaces the icosahedral phase in Al-Mn alloys. Crystallographic analysis of the process is also presented.

Occurrence of the Phases

In melt-spun ribbons of Al-Mn, the lowest Mn concentration at which the icosahedral phase appears is 15 wt%, and the decagonal phase appears when the Mn content reaches about 28 wt%. In alloys containing >28 wt% Mn, both icosahedral and decagonal phase are found, with the icosahedral phase being more abundant in the thinner (and thus more rapidly solidified) parts of the ribbons. Thus the thin parts of an Al-33.7 wt% Mn ribbon (corresponding to the formula Al_4Mn) are almost single phase icosahedral, while the thicker parts of ribbons with 35-37 wt% Mn are almost single phase decagonal. We have found that the addition of 5 wt% Si to Al-Mn alloys eliminates the formation of the decagonal phase, thus allowing easier formation of the icosahedral phase. In contrast, the addition of 5 wt% Ge to the alloys favors the formation of the decagonal phase.

In melt-spun Al-Mn alloys which contain both icosahedral and decagonal phases, the decagonal phase is found to grow epitaxially on the surface of icosahedral phase dendrites (4). The icosahedral phase has the form of equiaxed dendritic grains with random orientations, and a grain size which depends on the local cooling rate within the ribbon. This structure implies that the icosahedral phase nucleates and grows in an undercooled melt, and recalescence will therefore lead to a decrease in solidification velocity as the solidified volume increases. When the growth becomes too slow to maintain the icosahedral phase formation, the decagonal phase nucleates on the surface of the icosahedral dendrites.

Electron beam surface melting experiments provide more detailed information on the relationship between the icosahedral and decagonal phases. In these experiments, an electron beam is scanned across the surface of a bulk sample to produce a travelling melt zone. The scan velocity can be varied from about 0.1 to 500 cm/sec, with a correspondingly wide range in microstructure. Although local solidification velocities or cooling rates often cannot be correlated precisely to the scan velocity, the sequence of microstructures with changing velocity can be clearly established. In the experiments reported here, melt scans were carried out on an Al-25 wt% Mn alloy at velocities between 0.5 and 200 cm/sec. At each velocity, a series of overlapping melt scans was used to build up a strip of rapidly solidified material approximately 5 mm wide. The samples were examined by x-ray diffraction, optical metallography, SEM and TEM.

In the 100 cm/sec scans, the icosahedral phase grows in the form of dendritic grains which are typically 20-30 μm in diameter, considerably larger than those found in melt-spun ribbons. Earlier studies of icosahedral dendrites growing in an Al-18 wt% Mn alloy (5) showed that they grew preferentially along the three-fold symmetry axes of the icosahedral structure. The resulting crystals have the overall shape of a hollow-faced pentagonal dodecahedron (PD), and appropriately oriented examples show a conspicuous pentagonal symmetry. The same morphology is observed in the 100 cm/sec scans of the Al-25 wt% Mn alloy (Fig. 1). These crystals grow from nuclei within the melt zone, where significant supercoolings can develop because of the large driving force needed to produce rapid solidification of the equilibrium phases. Both x-ray diffraction and TEM confirm this structure as icosahedral. When higher cooling rates lead to a higher density of icosahedral grains, the full morphology of the PD dendrites does not have a chance to develop and the icosahedral phase must be identified by other characteristics.

In 25 cm/sec melts, roughly equal amounts of icosahedral and decagonal phase are present. The decagonal phase is always present as an overgrowth on the icosahedral phase, in many cases completely enveloping it (Fig. 2). Moreover, the icosahedral phase in many cases consists of remnants of a dendritic structure which has undergone significant decomposition.

At scan speeds of 2.5 cm/sec, much of the melt zone consists of decagonal phase crystals in the form of blocky cylinders about 1 μm in diameter and 2 μm long. The crystals are arranged in large dendrite-like colonies (Fig. 3), which typically extend for distances of 100 μm or more, but three factors show that they did not actually grow as large decagonal-phase dendrites. First, within any colony the decagonal phase is seen with a variety of orientations. Although the colonies are thus not single crystals like normal dendrites, the orientations are not random, but belong to a limited set of special orientations which will be discussed below. Second, most of the decagonal phase crystals within a colony do not appear to be interconnected except in a few areas where their density is so high that they have impinged on one another. Finally, the overall symmetry of the dendrite pattern frequently shows a pentagonal alignment (Fig. 4) or a pentagonal "shadow" (Fig. 5) highly reminiscent of the icosahedral crystals seen in the 100 cm/sec scan (Fig. 1). These features leave little doubt that this microstructure grew initially as large icosahedral dendrites with PD morphology, upon which decagonal phase crystals nucleated epitaxially. The decagonal phase then grew into the liquid and also into the icosahedral solid, consuming essentially all of the latter.

Crystallography of Decagonal Phase Growth

In a recent crystallographic analysis (6) it was concluded on the basis of transmission electron microscopy tilting experiments and convergent beam diffraction that the decagonal phase has a noncrystallographic point group symmetry ($10/m$ or $10/mmm$) different from icosahedral. The decagonal phase has a unique ten-fold rotation axis, and the electron diffraction pattern of a crystal viewed along this axis bears a strong similarity to that of an icosahedral crystal viewed along one of its five-fold axes. However, if we rotate the decagonal phase through the same angles (63.4°) which would bring the icosahedral phase to another of its five-fold axes, we find only a pseudo-ten-fold diffraction pattern in which rings of ten spots are seen, but the spots are commensurated to periodicity in one direction, as a result of the one-dimensional periodicity along the ten-fold axis. If one examines the zone lying 90 degrees from the decagonal phase's ten-fold axis, one observes electron diffraction patterns with two-fold symmetry at intervals of 18° . These two-fold patterns alternate between types referred to in ref. (3) as B and C. The presence of a unique ten-fold axis implies that planes normal to this axis are either quasiperiodic (like Penrose tiling), or multiply twinned. The second possibility was rejected on the basis of microdiffraction, dark field, and high-resolution imaging experiments. Figure 6 shows a high resolution image along the ten-fold axis, where no isolated crystalline (periodic) domains can be observed. However, an optical diffractogram (c) taken from selected small regions reproduces a pattern with ten-fold symmetry similar to an electron diffraction pattern (b).

Although the decagonal phase was found to be quasiperiodic within the planes normal to its ten-fold axis, the planes (layers) are stacked with 1.24 nm periodicity, as was shown by diffraction and high resolution imaging with the incident beam normal to the ten-fold axis (4). The conclusion was that the decagonal phase is a quasicrystal with two-dimensional quasiperiodicity and one-dimensional periodicity, with long-range decagonal orientational order.

The cylindrical growth morphology of the decagonal phase is consistent with the cylindrical symmetry $10/m$: the ten-fold rotation axis is along the cylinder axis, which is also probably the growth direction. The orientation relationship between the icosahedral and decagonal phases is presented in Fig. 7. Fig. 7a shows a high-resolution TEM image of the two phases, separated by a sharp interface. A selected area diffraction pattern of this area shows an overlapping of the two-fold pattern of the icosahedral phase on the two-fold (type B (3)) pattern of the decagonal phase (with typical streaking and periodicity, Fig. 7b). The unique ten-fold axis c^* of the decagonal phase coincides with one of the six five-fold axes of the icosahedral phase. The two-fold axes of the decagonal phase (zone axis of pattern B, (3)) coincide with one of the ten two-fold axes of the icosahedral phase, normal to the five-fold axis. Mirror planes of the two-fold pattern are rotated 31.7° . Fig. 7c represents the orientation relationship on a stereographic projection.

Growth of the icosahedral phase on the decagonal phase would give only one orientational variant, according to the established orientation relationship. However, growth of the decagonal phase on the icosahedral phase provides six orientational variants, and the ideal expected morphology is as shown in Fig. 8. The presence of the six orientational variants of the decagonal phase implies the presence of the icosahedral phase, at least at an earlier stage of the growth. Fig. 9 is a TEM image of a microstructure in a 10 cm/s melt, showing blocky crystallites of the decagonal phases embedded in aluminum. When a central rounded crystallite A was oriented with its ten-fold zone axis exactly parallel to the microscope's electron beam (diffraction pattern A), surrounding decagonal crystallites with typical striation contrast showed diffraction patterns with pseudo-ten-fold symmetry. Therefore, the unique ten-fold axes of the surrounding crystallites are 63.4° from the zone axis of crystallite A, and thus all of the decagonal crystals have ten-fold axes which coincide with the five-fold axes of an underlying icosahedral crystal. This corresponds exactly to the growth model of Fig. 8.

Analysis of an Al-27 wt% Mn melt-spun ribbon, which consisted entirely of the decagonal phase, showed that a similar crystallographic relationship existed between nearby grains. Specifically, if one grain was aligned so that the electron beam lay along its unique ten-fold axis, adjacent grains were found to show the pseudo-ten-fold axes (Fig. 10). The conclusion is that all of the grains originated by epitaxial nucleation from an initial icosahedral grain, which then completely disappeared.

Discussion

The morphology of the icosahedral and decagonal phase crystals in the electron beam surface melts indicates that the icosahedral phase nucleates and grows within the supercooled liquid of the melt zone, and the decagonal phase subsequently nucleates epitaxially on the icosahedral phase. The decagonal phase then grows and consumes the icosahedral phase. In 100 cm/sec melt scans, solidification is complete before the decagonal phase can make significant growth, and the icosahedral dendrites are therefore preserved. At 25 cm/sec, the icosahedral dendrite structure shows significant decomposition, and at 2.5 cm/sec sufficient time is available for the decagonal phase to completely replace the icosahedral dendrites. In the slower melts, however, the initial solidification of the icosahedral phase is clearly revealed by the spatial and orientational arrangement of the decagonal crystals. No microstructures were observed in the melt trails which could be interpreted as independently nucleating and growing decagonal phase.

The decagonal material found in melt spun ribbons of Al-Mn alloys appears to have originated by a similar mechanism of epitaxial nucleation on the icosahedral phase. In the 37 wt% Mn ribbon, the only evidence that the icosahedral phase was present at an earlier stage of crystallization is the presence of the orientational variants of the decagonal phase, which are related to one another by icosahedral symmetry.

The sequence of events in a supercooled Al-Mn melt thus appears to be an initial nucleation and rapid growth of icosahedral phase dendrites, followed by copious heterogeneous epitaxial nucleation of the decagonal phase. The decagonal phase then grows into both the liquid and the icosahedral phase, and if the solidification process is slow enough the icosahedral phase is completely eliminated.

This process is superficially similar to a peritectic reaction, but it appears to have some important differences. Thus although the icosahedral phase forms first and it is subsequently replaced by the decagonal phase, annealing experiments show that the decagonal phase is stable to higher temperatures than is the icosahedral phase. The sequence of events is thus determined not by the changing relative stability of the phases as the temperature changes, but by the sequence of nucleation processes. Thus the icosahedral phase nucleates most readily from the supercooled liquid, perhaps because of icosahedral clustering within the liquid (7) whereas the nucleation rate of the decagonal phase within the liquid is negligible. The icosahedral phase then forms a favorable substrate for the epitaxial nucleation of the decagonal phase. The decagonal phase is more stable than the icosahedral phase and grows to replace it.

Acknowledgement

The authors thank DARPA for financial support of this work, F. S. Biancanello for alloy preparation and C. Olson for SEM work.

References

1. D. Shechtman and I. Blech, *Met. Trans.* **16A**, 1005 (1985).
2. D. Shechtman, I. Blech, D. Gratias, and J. W. Cahn, *Phys. Rev. Lett.* **53**, 1951 (1984).
3. L. Bendersky, *Phys. Rev. Lett.* **55**, 1461 (1985).
4. L. Bendersky, R. J. Schaefer, F. S. Biancanello, W. J. Boettinger, M. J. Kaufman, and D. Shechtman, *Scripta Met.* **19**, 909 (1985).
5. R. J. Schaefer, L. A. Bendersky, D. Shechtman, W. J. Boettinger, and F. S. Biancanello, to be published.
6. L. Bendersky and M. J. Kaufman, to be published.
7. S. Sachdev and D. R. Nelson, *Phys. Rev. B* **32**, 4592 (1985).

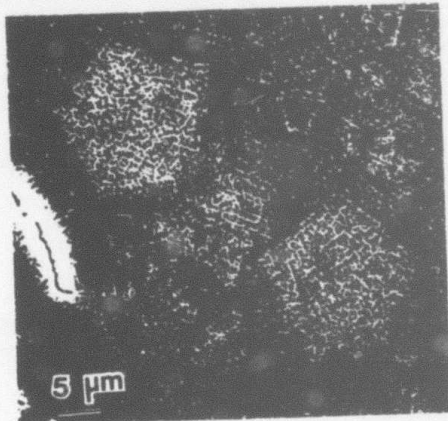


FIG. 1

Icosahedral dendrites in an Al-25 wt% Mn alloy electron beam melt scan. Scan velocity 100 cm/sec.

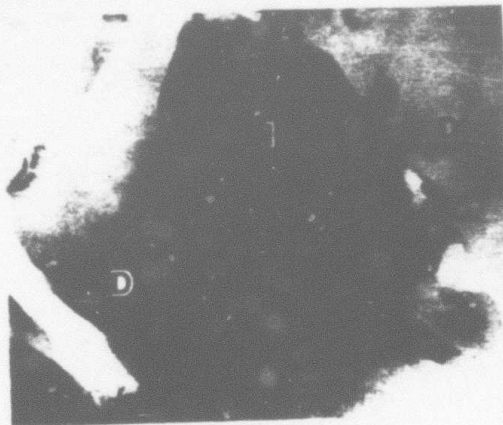


FIG. 2

Decagonal phase overgrowth on the icosahedral phase in a 25 cm/sec melt scan.

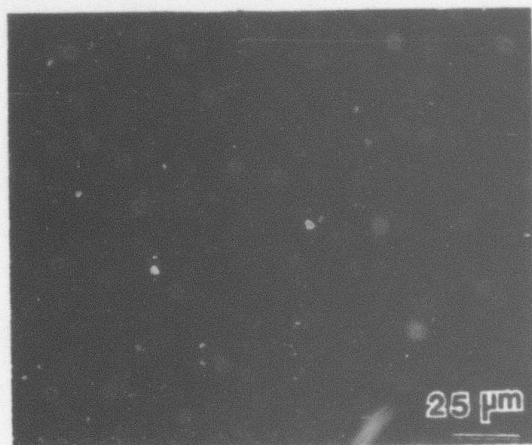


FIG. 3

Dendrite-like colonies of decagonal crystals in a 2.5 cm/sec melt scan.

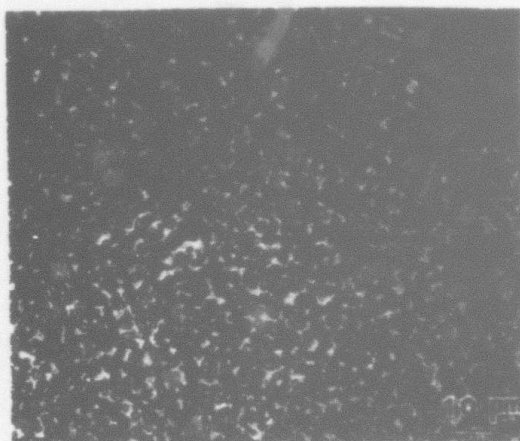


FIG. 4

Pentagonal alignment of decagonal phase crystals in a 2.5 cm/sec melt scan.

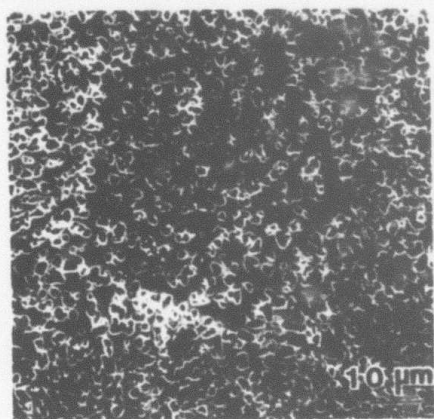


FIG. 5

Pentagonal "shadow" among decagonal crystals of a 2.5 cm/sec melt scan.

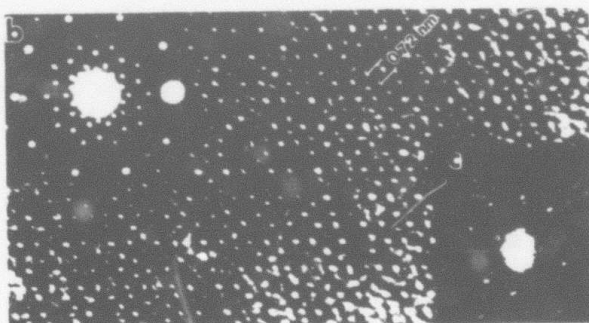


FIG. 6

High-resolution image of the decagonal phase viewed along its ten-fold axis, with electron diffraction pattern (b) and optical diffractogram (c).

FIG. 7

(a) High-resolution image of decagonal phase growing on the icosahedral phase. (b) Diffraction pattern of icosahedral and decagonal phases. (c) Superimposed stereographic projections of the icosahedral and decagonal phases. C^* is the ten-fold axis.

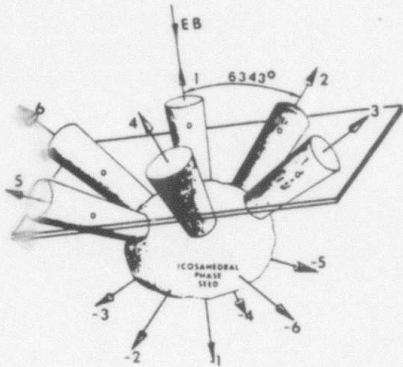


FIG. 9

Decagonal phase crystallites in a 10 cm/sec melt scan, with a central crystallite (A) showing 10-fold symmetry while surrounding crystallites show the pseudo-ten-fold symmetry.

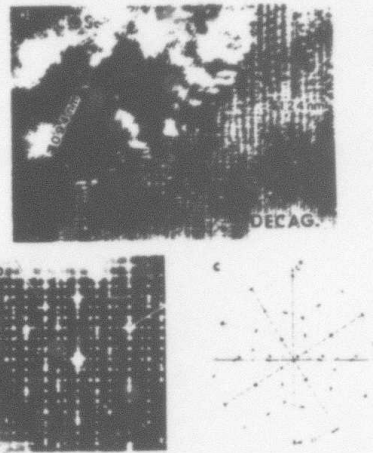
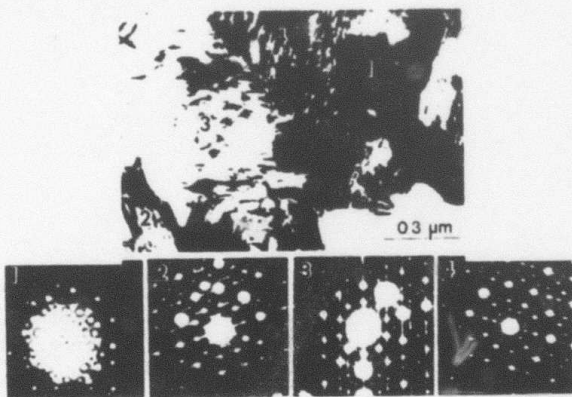


FIG. 8

Growth morphology resulting from nucleation of decagonal phase on the icosahedral phase according to the orientation relationship indicated in Fig. 7.

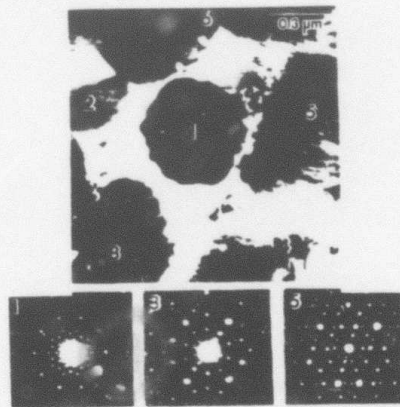


FIG. 10

Decagonal grains in melt-spun ribbon of Al-37 wt% Mn, oriented according to the pattern shown in Fig. 8.

PHIL. MAG. LETTERS

Determination of the point group of the icosahedral phase in an Al-Mn-Si alloy using convergent-beam electron diffraction

By L. A. BENDERSKY† and M. J. KAUFMAN

National Bureau of Standards, Gaithersburg, Maryland 20899, U.S.A.

[Received 30 September 1985 and accepted 17 December 1985]

ABSTRACT

Convergent-beam electron diffraction has been used to determine conclusively the point group of the icosahedral phase in an Al-Mn-Si alloy. The patterns obtained clearly display the symmetries expected for the orientations of a quasicrystalline phase with the $m\bar{3}5$ point group.

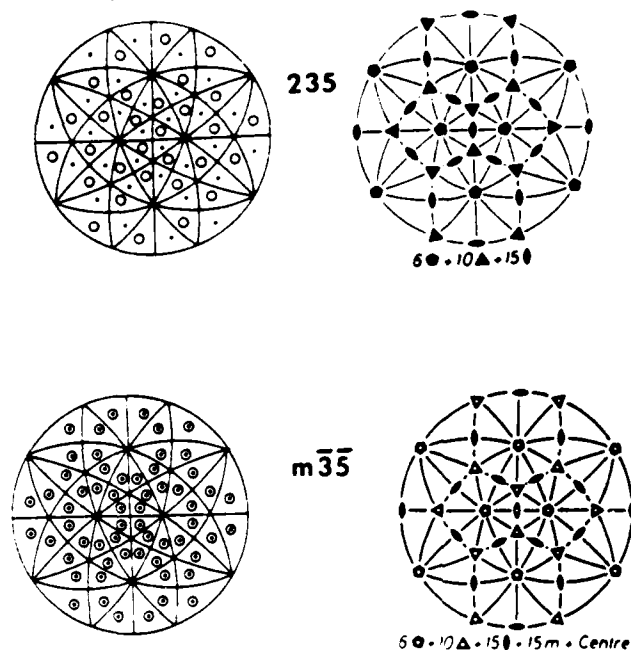
§1. INTRODUCTION

The recent discovery (Shechtman, Blech, Gratias and Cahn 1984) of a non-crystallographic icosahedral phase in rapidly solidified Al-Mn alloys has created considerable interest and controversy among the scientific community. The original identification of this phase was based primarily on the analysis of a series of selected-area diffraction patterns (SADPs) obtained in a transmission electron microscope; from the series of SADPs, Shechtman, *et al.* (1984) concluded that the point group of this phase was $m\bar{3}5$. However, the other possible icosahedral point group, 235 , could not be ruled out since SADPs from the major zone axes should appear similar. This is seen by considering fig. 1 (taken from *International Tables for Crystallography*, 1983) which shows the stereograms displaying the symmetry elements and the general points for the two icosahedral point groups, 235 of order 60 and $m\bar{3}5$ of order 120. Even though the symmetries of the special projections for these two point groups are different along $[1r0]$ (the fivefold axis) and $[111]$ (the threefold axis), due to Friedel's law, the projection diffraction symmetries for any of these orientations are identical (see table 1). Thus, it is impossible to distinguish between the two point groups using only the projection information obtained in SADPs.

The convergent-beam electron diffraction (CBED) technique has been shown to be extremely valuable for determining the point and space groups of crystalline phases (Buxton, Eades, Steeds and Rackham 1976, Steeds 1979, Kaufman and Fraser 1985). However, CBED patterns of sufficient quality for structure determination could not be obtained from the icosahedral phase in the binary alloys (Bendersky 1985, Gronsky, Krishnan and Tanner 1985), i.e. the patterns never contained the higher-order Laue

† Also with Center for Materials Research, The Johns Hopkins University, Baltimore, Maryland 21218, U.S.A.

Fig. 1



Stereographic projections of the symmetry elements and general points of the two icosahedral point groups, 235 and $m\bar{3}5$.

zone (HOLZ) information necessary for symmetry determination; arose from the presence of considerable internal strain in the icosahedral phase. In the present study, the CBED technique has been used successfully to study the symmetry of the icosahedral phase present in a ternary Al-Mn-Si alloy which had been rapidly solidified by a melt-spinning process. As will be shown, the convergent-beam patterns (CBPs) obtained provide sufficient HOLZ information both to conclude that this phase is truly icosahedral in nature and make it possible to discriminate between the two possible icosahedral point groups, 235 and $m\bar{3}5$.

§2. EXPERIMENTAL DETAILS

Melt-spun flakes of binary Al-25 wt.% Mn and ternary Al-38 wt.% Mn-5 wt.% Si were prepared from pre-alloyed ingots by melt spinning using a Cu wheel rotating at approximately 7000 r.p.m. The resulting rapidly solidified material was prepared for transmission electron microscopy by standard electropolishing methods using a solution of 10 parts (by volume) sulphuric acid and 90 parts methanol. Both single- and two-sided jet polishing were utilized. In addition, some of the flakes were argon-ion thinned using standard procedures. Subsequently, the thinned flakes were examined by analytical electron microscopy at 120 keV.

Table 1. Symmetries of the three major zone axes for the two icosahedral point groups, 235 and $m\bar{3}5$.

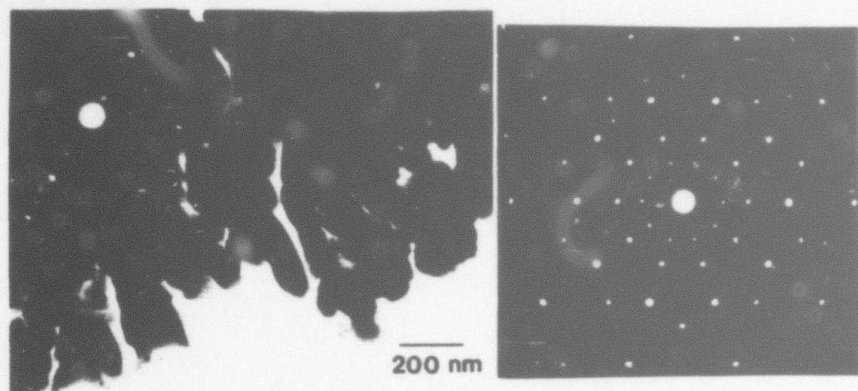
Point group	Fivefold axis [1 \bar{r} 0]	Threefold axis [111]	Twofold axis [001]
<i>Symmetry of special projections</i>			
235	5m	3m	2mm
$m\bar{3}5$	10mm	6mm	2mm
<i>Projection diffraction symmetry</i>			
Both	10mm	6mm	2mm

§3. RESULTS AND DISCUSSION

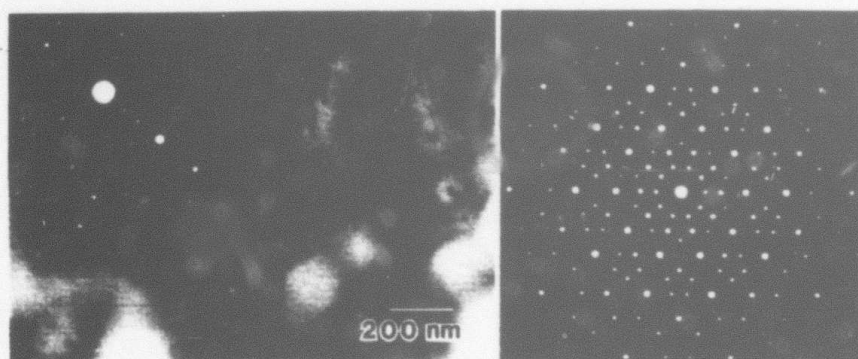
Before discussing the convergent-beam analysis of the icosahedral phase in the ternary alloy, it is instructive to compare the microstructures and SADPs from this phase with the binary Al-Mn results. For example, in fig. 2 the microstructures and SADPs obtained from the icosahedral phase in the two alloys are shown. It can be seen that the phase in the ternary alloy displays significantly less strain-contrast. However, weak-beam dark-field (WBDF) images indicated that the background 'speckling'—suggesting the presence of very fine crystallites that are twin related (Field and Fraser 1984)—was present in both alloys. In addition, it can be seen that the relative intensities in the SADPs have changed significantly indicating that the Si addition apparently has affected the order of the icosahedral phase in some way. Chen and Chen (1985) reported a similar effect, which they attributed to an increased ordering caused by the Si and suggested that the new quasicrystalline structure was a 'superlattice' of that in the binary Al-Mn alloys obtained by scaling the three- and fivefold patterns by the golden mean $\tau = (1 + \sqrt{5})/2$ (the characteristic number of icosahedral quasiperiodicity) and the twofold patterns by a non-uniform scaling factor. An alternative explanation is that the Si addition simply modifies the structure factors of the reflections from the same quasilattice.

Presumably because of the increased degree of order (or decreased internal strain) of the icosahedral phase in the ternary alloys, the CBPs obtained from various zone axes were found to contain sufficient three-dimensional information (i.e. HOLZ lines and reflections) for deducing the diffraction group and, finally, the point group. Figure 3 shows pairs of CBPs (low and medium camera length) for the five-, three- and twofold zone axes. For the fivefold axis (fig. 3(a)) it can be seen that the projection diffraction symmetry is 10mm and the whole pattern symmetry is 5m. This corresponds to the diffraction group $10_r mm_r$ (using the notation of Buxton *et al.* (1976)). The projection diffraction and whole pattern symmetries for the threefold and twofold axes (fig. 3(b) and (c)) are respectively 6mm and 3m, and 2mm and 2mm; for the threefold axis these symmetries correspond to the diffraction group, $6_r mm_r$, while the diffraction group for the twofold axis is either 2mm or $2mm 1_r$. The diffraction groups expected for these three orientations are given in table 2 for the two possible icosahedral point groups, 235 and $m\bar{3}5$. It is clear that the only consistent point group is $m\bar{3}5$.

Fig. 2



(a)



(b)

Bright-field electron micrographs and SADPs from the icosahedral phase: (a) Al-25 wt.%, Mn; (b) Al-38 wt.%, Mn-5 wt.% Si.

Table 2. Diffraction groups of the three major zone axes for the two icosahedral point groups, $\bar{2}35$ and $m\bar{3}5$.

Point group	Fivefold axis [1 τ 0]	Threefold axis [111]	Twofold axis [001]
$\bar{2}35$	$5m_R$	$3m_R$	$2m_R m_R$
$m\bar{3}5$	$10_R m m_R$	$6_R m m_R$	$2m m 1_R$

Table 1. Symmetries of the three major zone axes for the two icosahedral point groups, $\overline{235}$ and $\overline{m35}$.

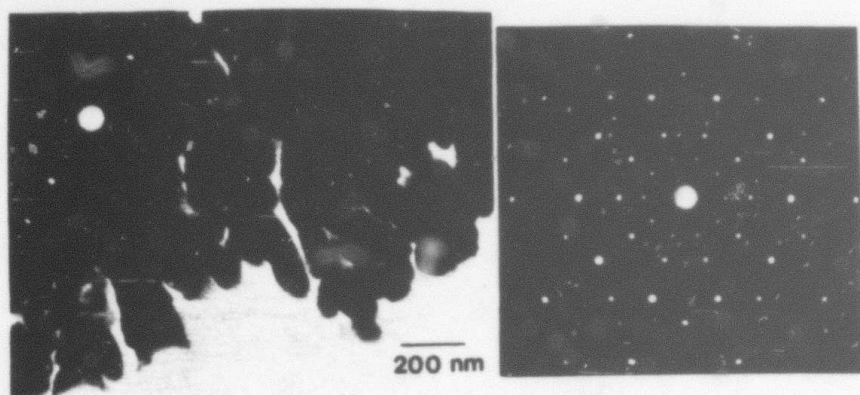
Point group	Fivefold axis [1 τ 0]	Threefold axis [111]	Twofold axis [001]
<i>Symmetry of special projections</i>			
$\overline{235}$	5m	3m	2mm
$\overline{m35}$	10mm	6mm	2mm
<i>Projection diffraction symmetry</i>			
Both	10mm	6mm	2mm

§ 3. RESULTS AND DISCUSSION

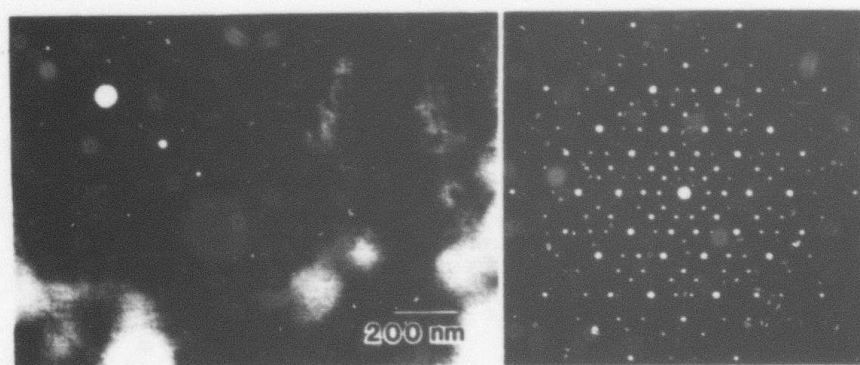
Before discussing the convergent-beam analysis of the icosahedral phase in the ternary alloy, it is instructive to compare the microstructures and SADPs from this phase with the binary Al-Mn results. For example, in fig. 2 the microstructures and SADPs obtained from the icosahedral phase in the two alloys are shown. It can be seen that the phase in the ternary alloy displays significantly less strain-contrast. However, weak-beam dark-field (WBDF) images indicated that the background 'speckling'—suggesting the presence of very fine crystallites that are twin related (Field and Fraser 1984)—was present in both alloys. In addition, it can be seen that the relative intensities in the SADPs have changed significantly indicating that the Si addition apparently has affected the order of the icosahedral phase in some way. Chen and Chen (1985) reported a similar effect, which they attributed to an increased ordering caused by the Si and suggested that the new quasicrystalline structure was a 'superlattice' of that in the binary Al-Mn alloys obtained by scaling the three- and fivefold patterns by the golden mean $\tau = (1 + \sqrt{5})/2$ (the characteristic number of icosahedral quasiperiodicity) and the twofold patterns by a non-uniform scaling factor. An alternative explanation is that the Si addition simply modifies the structure factors of the reflections from the same quasilattice.

Presumably because of the increased degree of order (or decreased internal strain) of the icosahedral phase in the ternary alloys, the CBPs obtained from various zone axes were found to contain sufficient three-dimensional information (i.e. HOLZ lines and reflections) for deducing the diffraction group and, finally, the point group. Figure 3 shows pairs of CBPs (low and medium camera length) for the five-, three- and twofold zone axes. For the fivefold axis (fig. 3(a)) it can be seen that the projection diffraction symmetry is 10mm and the whole pattern symmetry is 5m. This corresponds to the diffraction group $10_r mm_r$ (using the notation of Buxton *et al.* (1976)). The projection diffraction and whole pattern symmetries for the threefold and twofold axes (fig. 3(b) and (c)) are respectively 6mm and 3m, and 2mm and 2mm; for the threefold axis these symmetries correspond to the diffraction group $6_r mm_r$, while the diffraction group for the twofold axis is either 2mm or $2mm 1_r$. The diffraction groups expected for these three orientations are given in table 2 for the two possible icosahedral point groups, $\overline{235}$ and $\overline{m35}$. It is clear that the only consistent point group is $\overline{m35}$.

Fig. 2



(a)



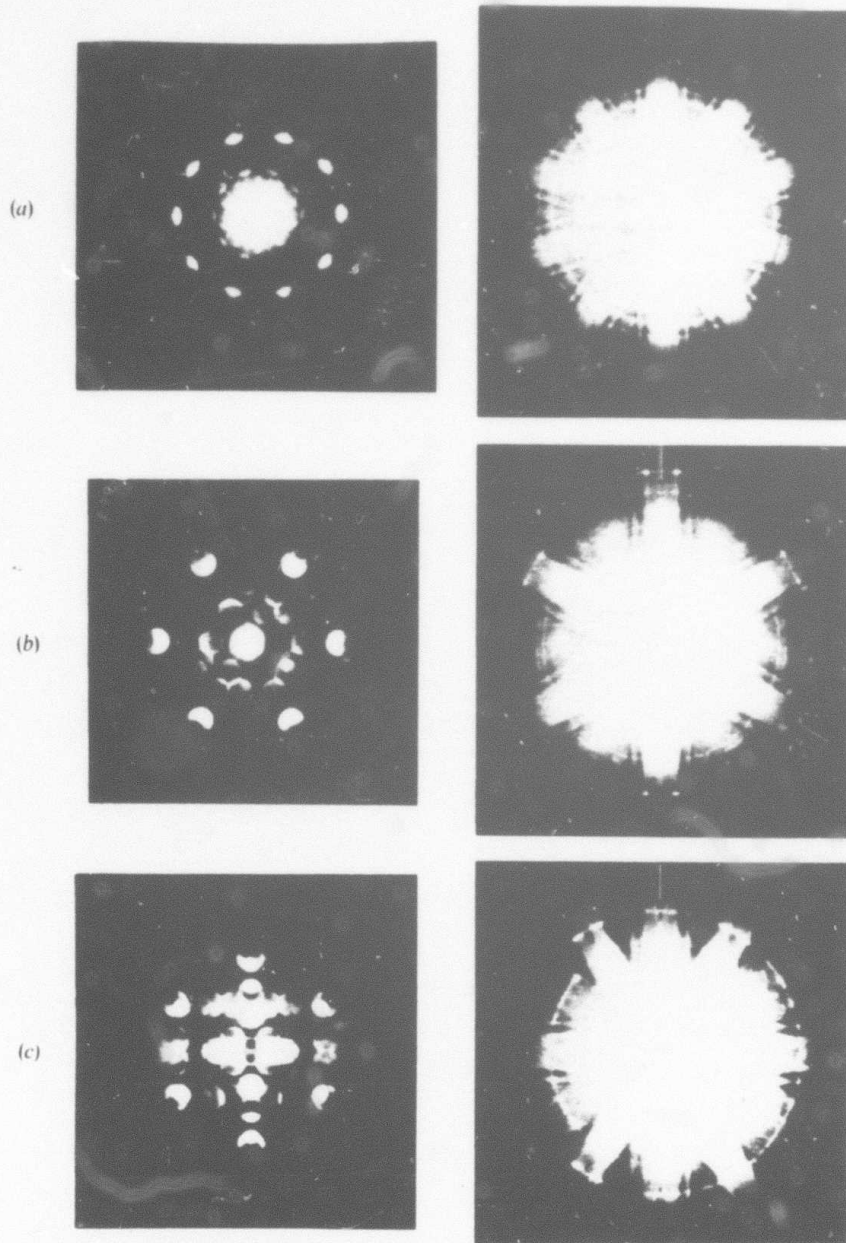
(b)

Bright-field electron micrographs and SADPs from the icosahedral phase: (a) Al-25 wt.%, Mn;
(b) Al-38 wt.%, Mn-5 wt.%, Si.

Table 2. Diffraction groups of the three major zone axes for the two icosahedral point groups, 235 and $m35$.

Point group	Fivefold axis [1 τ 0]	Threefold axis [111]	Twofold axis [001]
235	$5m_R$	$3m_R$	$2m_R m_R$
$m35$	$10_R m m_R$	$6_R m m_R$	$2m m 1_R$

Fig. 3



CBPs from the icosahedral phase in the Al-38 wt.% Mn-5 wt.% Si ribbon: (a) fivefold (b) threefold and (c) twofold. The lines in the low-camera-length patterns indicate the mirror planes.

Finally, it is possible to make measurements of the spacings of the higher-order Laue zone rings and convert the values to reciprocal-lattice spacings along the major directions. The results obtained indicate that the spacing of the reciprocal-lattice planes are non-periodic as expected for the quasiperiodic lattice of the icosahedral phase (Levine and Steinhardt 1984). For example, for the twofold CBP (fig. 3(c)) the spacing (H) of the first three reciprocal-lattice planes normal to the beam direction, are approximately in the τ ratio, i.e. $H_{\text{SOLZ}}/H_{\text{FOLZ}} \cong 1.58$ and $H_{\text{TOLZ}}/H_{\text{SOLZ}} \cong 1.61$ where FOLZ, SOLZ and TOLZ stand for first-order Laue zone, second-order Laue zone and third-order Laue zone, respectively. Further implications suggested by these spacings will be discussed in a separate paper.

From the preceding discussion, it is clear that the structure of the phase of interest in Al-Mn and Al-Mn-Si alloys is non-crystallographic, with the $m\bar{3}5$ point group. However, it is informative to discuss the real/reciprocal space relationship of the icosahedral phase. For example, the symmetries of a crystalline structure and its Fourier transform (reciprocal lattice) are identical, i.e. the point symmetry of any lattice point is equivalent to that of any reciprocal-lattice point. The symmetry of the Fourier transform of a quasiperiodic structure however, will differ significantly from that of the actual structure and its quasilattice; the high symmetries of the diffraction patterns obtained from the icosahedral phase are not equivalent to the symmetries of the atomic species in real space. In fact, it has been suggested that it is the average properties of the structure in real space which have icosahedral symmetry and not the atomic species (Gratias and Cahn 1985).

In conclusion, it has been shown using CBED that the structure of the complex phase observed in Al-Mn and Al-Mn-Si alloys is icosahedral and has the point group $m\bar{3}5$, instead of the alternative, 235 . Also, it appears that the addition of Si has increased the perfection of the icosahedral phase, indicating that the 'speckling' observed in WBDF images may not result from very-short-range internal strains.

ACKNOWLEDGMENTS

The authors are grateful to R. Spall for valuable discussions, F. S. Biancianiello for producing the melt-spun ribbons and D. Carrick for TEM specimen preparation. One of us, L. A. B., thanks the DARPA for financial support of this work.

REFERENCES

- BENDERSKY, L., 1985, *Phys. Rev. Lett.*, **55**, 1461.
 BUXTON, B. F., EADES, J. A., STEEDS, J. W., and RACKHAM, G. M., 1976, *Phil. Trans. R. Soc. Lond.*, **A281**, 171.
 CHEN, C. H., and CHEN, H. S., 1985, *Phys. Rev. Lett.* (to be published).
 FIELD, R. D., and FRASER, H. L., 1985, *Mater. Sci. Engrng.* **68**, L17.
 GRATIAS, D., and CAHN, J. W., 1985, *Scripta Metallurgica* (to be published).
 GRONSKY, R., KRISHNAN, K., and TANNER, L., 1985, *Proceeding of 43rd Annual EMSA Meeting*, edited by C. V. Bailey (San Francisco Press), p. 34.
International Tables for Crystallography, 1983, edited by T. Hahn (Boston: D. Reidel Publ. Co.), Vol. A, pp. 778-789.
 KAUFMAN, M. J., and FRASER, H. L., 1985, *Acta metall.*, **33**, 191.
 LEVINE, D., and STEINHART, P. J., 1984, *Phys. Rev. Lett.*, **53**, 2477.
 SHECHTMAN, D., BLECH, I., GRATIAS, D., and CAHN, J. W., 1984, *Phys. Rev. Lett.*, **53**, 1951.
 STEEDS, J. W., 1979, *Introduction to Analytical Electron Microscopy* (New York: Plenum Press), p. 387.

Nucleation behavior of Al-Mn icosahedral phase

L. A. Bendersky* and S. D. Ridder

Metallurgy Division, National Bureau of Standards, Gaithersburg, Maryland 20899

(Received 26 February 1986; accepted 14 April 1986)

Electrohydrodynamic (EHD) atomization has been used to rapidly solidify micron and submicron size droplets of Al-14 at. % Mn to study nucleation behavior of icosahedral phase. Icosahedral grain size has been found to decrease continuously with decreasing droplet size. Based on this result, formation of the icosahedral phase is explained by homogeneous nucleation. Extremely low resistance to nucleation of icosahedral phase can be understood if possible topological similarities between liquid and icosahedral quasicrystal are considered. Formation of glass as configurationally frozen liquid in Al-Mn and similar alloy systems is questionable, implying that the reported Al-Mn glass probably has a microquasicrystalline structure.

I. INTRODUCTION

Icosahedral phases have received extensive study in the last year. The phase was first discovered in rapidly solidified Al-Mn alloys by Shechtman *et al.*¹ and then in many other aluminum-transition metal systems.² Moreover, icosahedral phases now have been reported in several nonaluminum-based systems: $Mg_{32}(Al,Zn)_{49}$,³ Mg_4CuAl_6 ,⁴ Cd-Cu,⁵ Pd₃USi,⁶ $(Ti_{1-x}V_x)_2Ni$.⁷ A common feature of these phases is that in reciprocal space they exhibit sharp Bragg peaks but with icosahedral $m\bar{3}\bar{5}$ point group symmetry that implies that they cannot be crystals with lattice translational invariance. Several theoretical models have been developed to explain coexistence of a noncrystallographic point group and sharp diffraction,⁸⁻¹² all approaching an idea of quasiperiodic long-range translational order together with long-range orientational order. Accordingly, the term quasicrystal⁸ has been used for this material.

Long-range icosahedral order is known only for the recently discovered icosahedral phases. However, short-range icosahedral order (SRIO) is readily observed in condensed matter. Short-range icosahedral order is believed by many investigators to be a feature of metallic glasses and liquids.¹³⁻¹⁵ This topological property arises from energetic consideration of tetrahedral packing, as was made clear by Frank¹⁶ and confirmed by different structure models generated physically or by computer (citations in Ref. 14). Other types of structure having SRIO are Frank-Kasper phases¹⁷ characterized by unusually large unit cells and described as combinations of icosahedral with certain other polytetrahedral configurations.

These two predominantly polytetrahedral structures of glass and Frank-Kasper phases with SRIO were shown to be closely related in a theoretical analysis by Nelson.¹⁸ Both structures can be derived from ideal

tetrahedral packing, possible without frustration in three-dimensional curved space, by a disordered or periodically ordered arrangement of disclination lines. The possibility of a structural relationship between metallic glass and icosahedral quasicrystal was also discussed recently.¹⁹ Some experimental evidence of this possible structural interrelation of metallic glasses, Frank-Kasper phases, and the newly discovered icosahedral phase was found recently:

(1) Most of the discovered icosahedral phases mentioned above form in systems and compositional ranges where the equilibrium phases are of the Frank-Kasper type. The structure of some of these phases can be successfully decomposed to the same building blocks used for icosahedral quasiperiodic lattice models.^{20,21}

(2) The formation of metallic glass at the composition of the icosahedral phase was claimed to be observed for the Al-Mn system, using different energy-assisted processes²²⁻²⁴ and for PdUSi (Ref. 6) by liquid quenching. For both systems a glass-to-quasicrystalline state

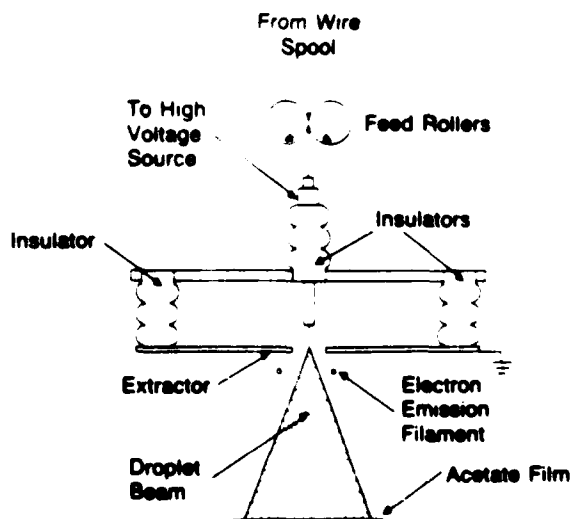


FIG 1 Schematic of experimental apparatus for electrohydrodynamic atomization.

* Also with the Center for Materials Research, The Johns Hopkins University, Baltimore, Maryland 21218.

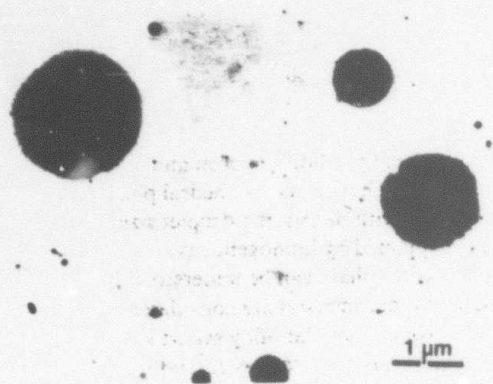


FIG. 2. TEM image of fine spherical particles of Al-26 wt. % Mn supported by amorphous carbon film.

transition was observed and for Al-Mn a quasicrystal-line-to-glass transition, using a combination of thermal annealing and energy-assisted processes (ion-beam or electron irradiation).

In the present work we explore the possibility of forming Al-Mn glass by liquid quenching, bypassing the formation of icosahedral phase by utilizing the high cooling rate achieved in the cooling of ultrafine liquid microparticles. The possible transition in formation from icosahedral phase to glass will be discussed. An understanding of this transition is important in view of the speculation about an "intermediate" state of quasicrystal between the glassy and crystalline states. Using the assessed parameter of degree of cooling rate, the nucleation behavior of the icosahedral phase is investigated.

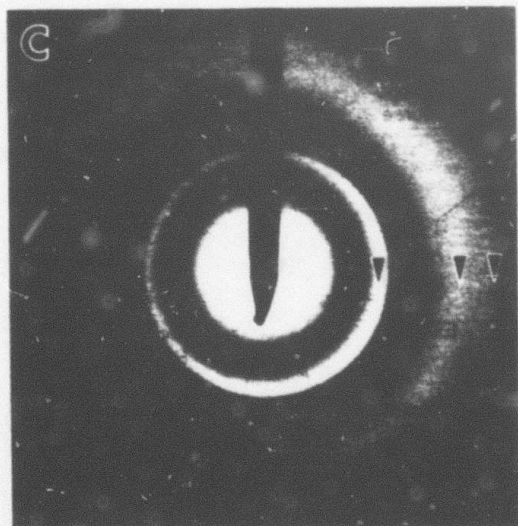
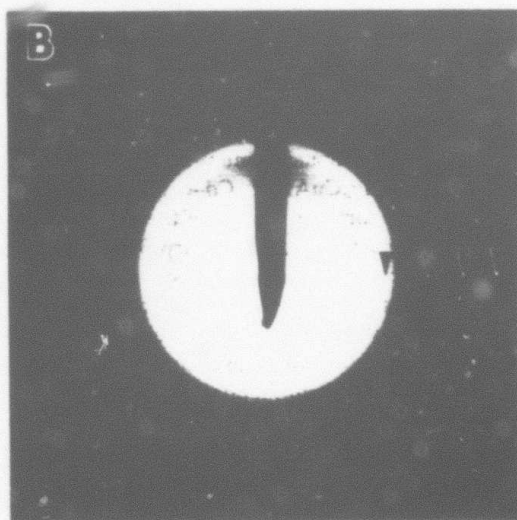
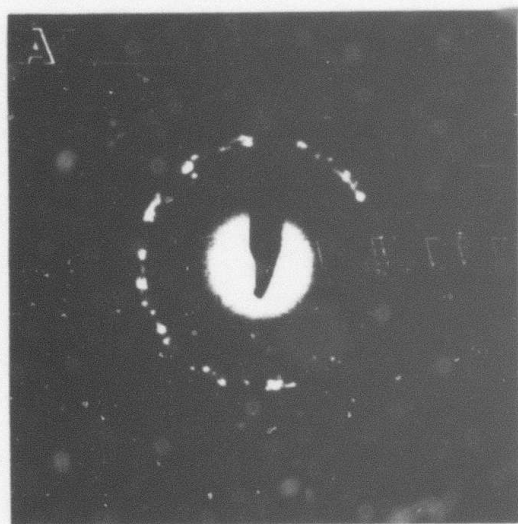


FIG. 3. Selected area electron diffraction patterns obtained for different particle size: (A) micron size, (B) half-micron size, (C) less than $0.1 \mu\text{m}$. Arrows show diffraction peaks of the same location.

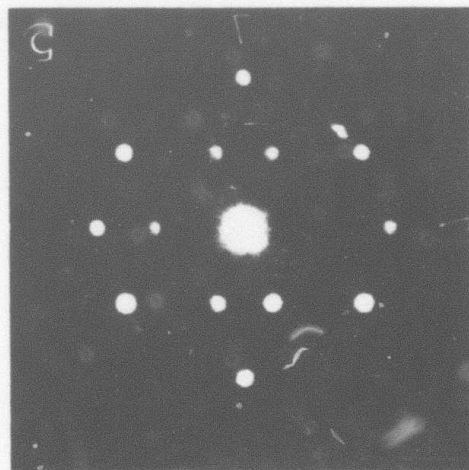
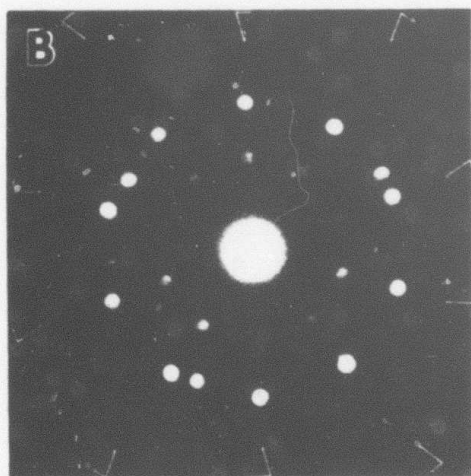
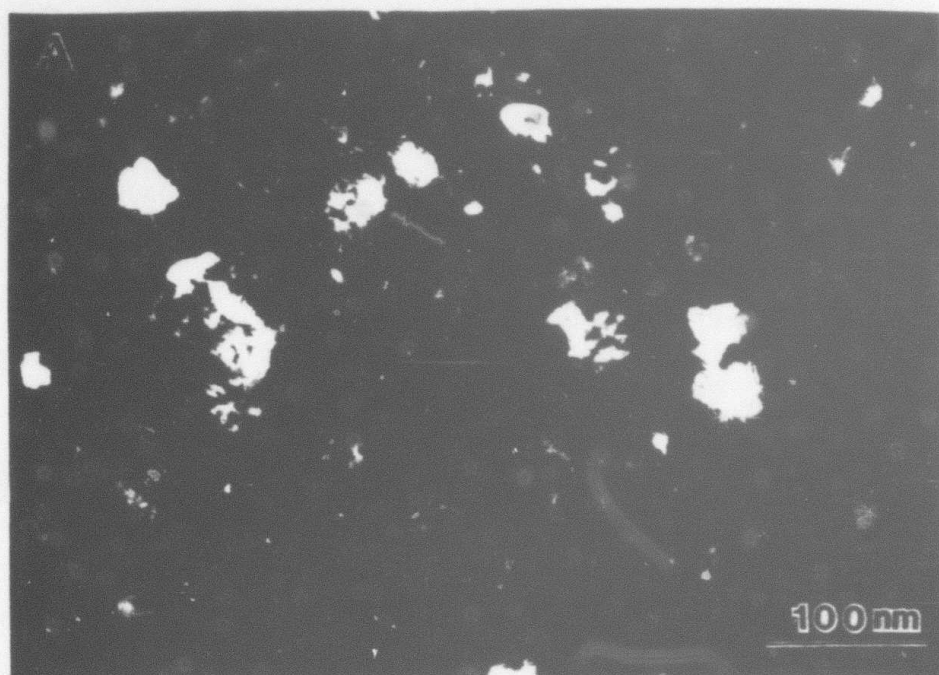


FIG. 4. Dark-field image of randomly oriented icosahedral grains (A). Microdiffractions with 20 nm probe show typical fivefold (B) and twofold (C) patterns of the icosahedral phase.

II. EXPERIMENTAL

Alloys for this study were produced by arc melting of 99.99% Al and 99.97% Mn to a nominal composition of Al-14 at. % Mn. The ultrafine particles were produced in a recently developed wire-feed version of EHD atomization.²⁵ In this version of EHD atomization a 1 mm diam wire of the desired composition is placed in a vacuum chamber ($<10^{-3}$ Pa) and fed through the

opening in an extraction plate via a capstan drive mechanism (see Fig. 1). Since the wire is held at a high positive potential (~ 15 kV), the ground referenced filament below the extractor, when heated, will emit a converging, cone-shaped, electron beam that melts the tip of the wire. The molten tip of the wire is formed into a spike due to the high electrostatic stress that disrupts it into very fine droplets in sizes ranging from 20 nm to 2 μm . The droplets travel approximately $\frac{1}{4}$ m before hit-

ting an acetate film placed at the bottom of the chamber. After removal from the vacuum, the film with the collected solidified particles is vapor coated with carbon and the acetate is dissolved in acetone. The microstructure of the particles was examined using a 300 keV transmission electron microscope (TEM) without any additional preparation. Because of the low atomic number of aluminum, the particles are sufficiently transparent in all ranges of sizes. *In-situ* heating experiments were performed, using a 120 keV focused electron beam, with the second condenser aperture out.

III. RESULTS

A. Microstructure of as-solidified microparticles

Figure 2 shows a typical low magnification image of solidified Al-14 at. % Mn particles embedded in a very thin amorphous carbon film. The spherical form of the particles shows that they solidified before hitting the substrate, because otherwise splats would be observed. Since the atomization chamber has a relatively high vacuum, the thermal history is determined primarily by radiation cooling. Accordingly, the smaller particles have a higher cooling rate and, for the same nucleation mechanism, a higher initial undercooling prior to crystallization. For the observed range of particle sizes from $2\ \mu\text{m}$ –20 nm, a range of at least two orders of magnitude in the cooling rate is expected.

In general, the particle microstructure consists of small randomly oriented grains [Fig. 7(0)] exhibiting Debye ring selected area electron diffraction (SAD) patterns [Fig. 3(A)]. These patterns can be indexed as a pattern of icosahedral quasicrystal, according to the six-index scheme.^{26,27} The result of microdiffraction from relatively large individual grains (~ 50 nm) confirms this: Figs. 4(B) and 4(C) show typical five- and twofold microdiffraction patterns of the icosahedral phase taken from grains shown on the dark-field image of Fig. 4(A). Selected area diffraction patterns from the largest particles ($1\text{--}2\ \mu\text{m}$ in size) also show a few reflections of fcc aluminum, absent in smaller particles.

As the size of the particles decreases, the Debye rings on the SAD pattern become continuous and diffuse [Fig. 3(B)]. For the smallest particles (less than 30 nm in diameter) the diffraction shows features typical of many metallic glasses: broad peaks with positions related by $q_2/q_1 = 1.7$ and $q_3/q_1 = 2.0$ [Fig. 3(C)], where q_1 is the strongest intensity peak.

To find a relationship between the characteristics of the diffraction patterns, particle size and microstructure (grain size), a number of dark-field images from different particles were taken, using the strongest ring(s) (q_1) reflections. The average size of the coherently reflecting zones was measured and plotted against the size of the corresponding particle. Figure 5 shows the re-

sults. In the particle size range between $2\ \mu\text{m}$ and 20 nm the size of the coherently reflecting zone *continuously* changes from 50 to $\sim 1\text{--}2$ nm. The ranges of particle sizes where the three types of SAD patterns (Fig. 3) were observed are also shown. Coherently reflecting zones larger than ~ 3 nm are grains of icosahedral quasicrystal. However, zones smaller than $3\text{--}2$ nm can be interpreted as the contrast effects of truly homogeneous amorphous material (i.e., dense random packing structure)^{28,29} or of microcrystalline (or microquasicrystalline in our case) material.^{30,31}

The icosahedral grain size (~ 50 nm) observed at $\sim 2\ \mu\text{m}$ particles is very close to that found on the chill surface of melt-spun ribbons. In the ribbons, the size of the icosahedral grains increases with increasing distance from the chill surface from ~ 70 nm up to $10\ \mu\text{m}$ in size, and in the largest grains a more developed dendritic structure is seen [Figs. 6(A) and 6(B)] (see also Refs. 32 and 34).

B. *In-situ* annealing

Since the particle microstructure described above is believed to be metastable, an *in-situ* annealing experiment was conducted in order to study the transformation to a more stable state. Figure 7 shows a series of images with corresponding SAD patterns, taken at different stages of a heating experiment. The initial micro-

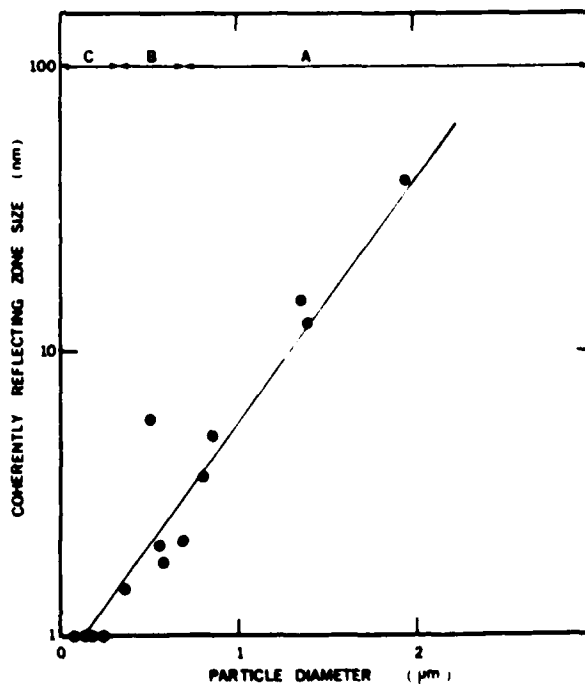


FIG. 5. Size of coherently reflecting zones plotted against particle diameter. A range of particle size where three typical SAD patterns A, B, and C are observed is also shown.

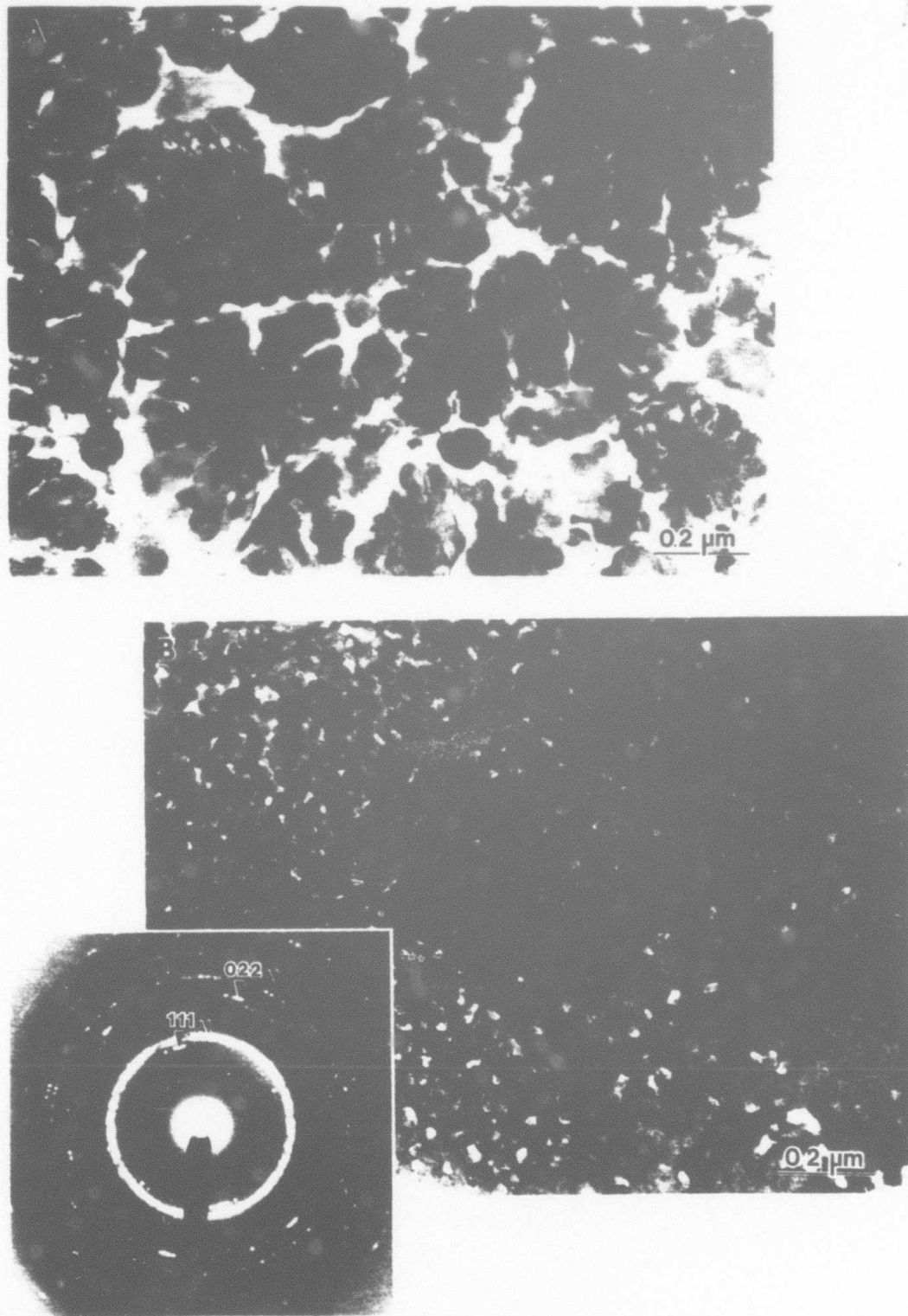
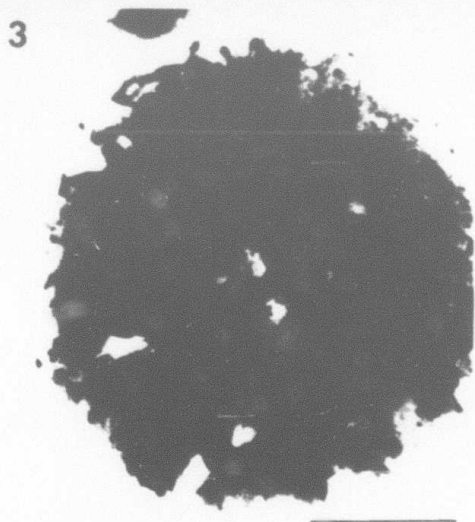
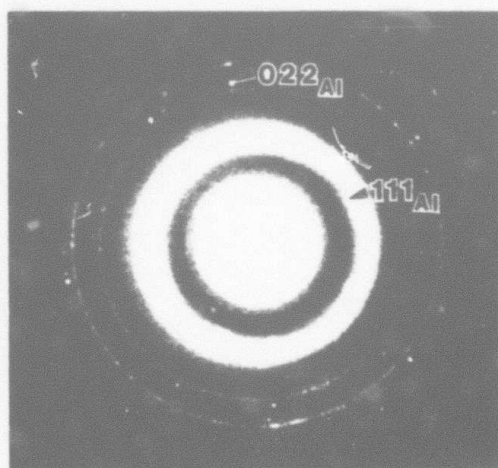
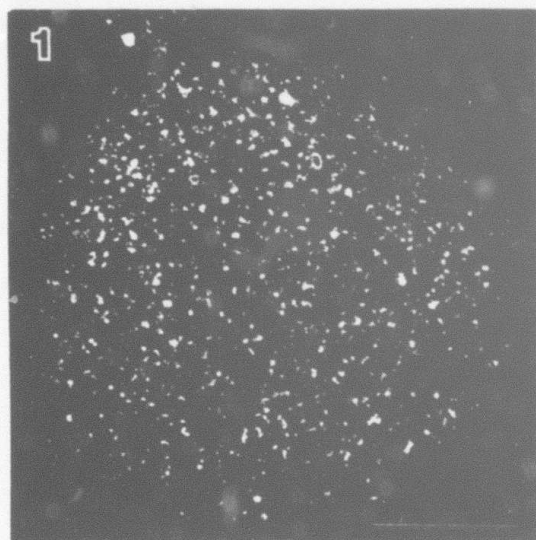
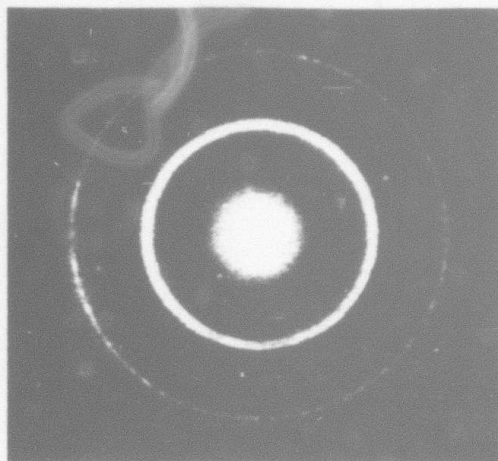
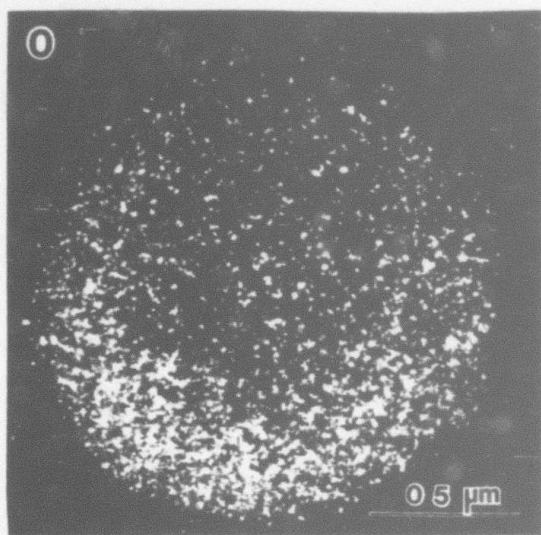


FIG. 6. Microstructure of icosahedral phase observed in melt-spun Al-26 wt. % Mn ribbons: (A) middle of the ribbon, (B) chill surface. Corresponding SAD patterns taken from 1 μm diam area are also shown.



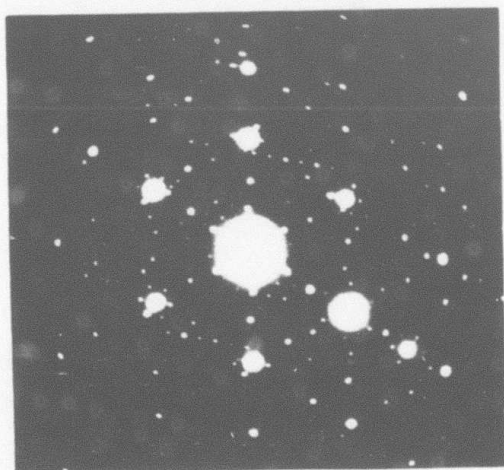
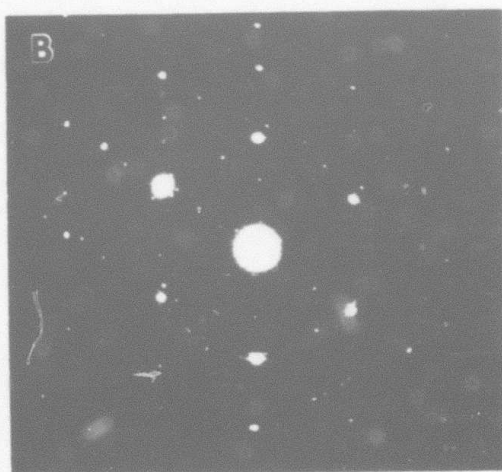
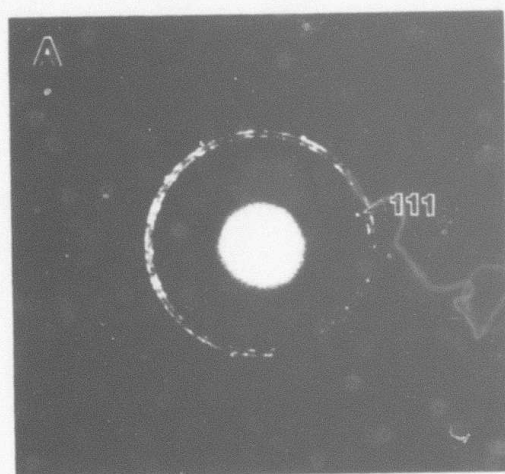
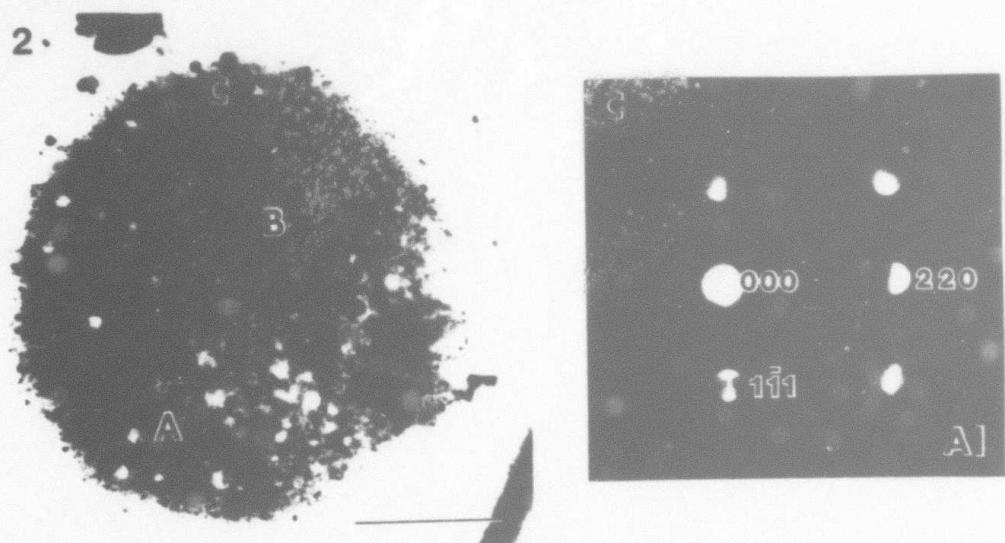


FIG. 7. Series of bright-dark-field images with corresponding SAD patterns, taken at different stages of *in-situ* heating. (0) is initial microstructure. (1) to (3) are different stages of progressive heating.

structure (0) of 1.6 μm particles consists of icosahedral grains 15–30 nm in size. According to the first SAD pattern, no fcc aluminum is detected. The first stage of heating (1) does not show any considerable change in grain size. However, smaller glass-type particles near the heated particle transform to a microquasicrystalline structure with roughly the same grain size as the studied particle. During this stage of heating fcc aluminum precipitates as small blocky grains (note individual spots belonging to fcc Al in the SAD pattern). An additional increase in temperature (stage 2) results in nucleation and growth of an ordered crystalline phase (region B) where the SAD pattern B is taken. Again, there is no coarsening of the remaining icosahedral grains but some coarsening of the aluminum grains is seen (see aluminum grain C and microdiffraction pattern taken from it). With additional heating, the crystalline phase proceeds to grow until it occupies the entire volume of the particle. In the final stage (3) the particle consists of a single grain of the crystalline phase (as shown by SAD pattern) with inclusions of aluminum grains that were eluded by a transformation front. The phase fragments into small domains by, probably, antiphase boundaries.

Analysis of the SAD patterns of the ordered crystalline phase shows that it is a new hexagonal phase different from any known hexagonal phases in the Al-Mn system. However, comparison of SAD patterns at the [0001] zone axis of this phase with the so-called Al_4Mn reveals similarities in the fundamental reflections but a difference in the superlattice ($a \approx 1.7$ nm of the new phase compared to $a = 2.84$ nm of Al_4Mn).³³ It is suggested that both phases are built from the same packing units but with different stacking order.

IV. DISCUSSION

Observation of the microstructure of Al-26 wt. % Mn melt-spun ribbons and EHD atomized particles shows a common mode of icosahedral phase formation over a wide range of cooling rates. The phase nucleates independently in an undercooled melt and grows outward until impingement with other grains occurs. The nucleation temperature and recalescence determine the composition of the icosahedral grains. For small grains (less than ~ 30 nm) the solidification is probably massive without rejection of aluminum. The metastable equilibrium composition of the icosahedral phase is believed to be close to Al_4Mn ,³⁴ and this is clearly seen during an annealing experiment where free aluminum was precipitated before transformation of the icosahedral phase took place. For larger grains (more than 100 nm) partitioning of aluminum takes place during solidification with subsequent development of dendritic growth. For the largest observed morphology of the dendrites was demonstrated.^{14,35}

The found dependence of the icosahedral grain size (d) on a geometrical parameter (particle size or distance from a wheel surface) can be interpreted as a dependence on the local cooling rate. The average cooling rate of the particles can be roughly estimated, assuming radiation cooling of the droplets,²⁵ at $\dot{T} = 2 \times 10^5 / D$ K/s, where D is the particle diameter in micrometers. Figure 8 represents the dependence of icosahedral grain size (d) (larger than 2 nm) on cooling rate (\dot{T}) (based on experimental data for particles, Fig. 5), approximated by a least-square fit to a straight line such that $d \propto (\dot{T})^{-1.7}$. Extrapolation of the curve to lower cooling rate range of melt spinning conditions (usually estimated as 10^4 – 10^5 K/s) satisfies roughly experimental data of the icosahedral grain size measured at different location of melt-spun ribbons ($\sim 1 \mu\text{m}$ in the middle of the ribbons and down to ~ 50 nm on the chill surface). This unique relationship and similarity of microstructure leads us to believe that the same nucleation mechanism operates over this broad range of conditions.

This copious nucleation of icosahedral phase demonstrates an extremely low resistance to nucleation. Copious nucleation from a melt can be promoted by the presence of a high density of catalytic impurities, or motes, and in such cases is heterogeneous. However, in the present study case of the icosahedral phase, the number of motes would have to be on the order of at least 10^{18} particles per cm^3 , which is many orders of

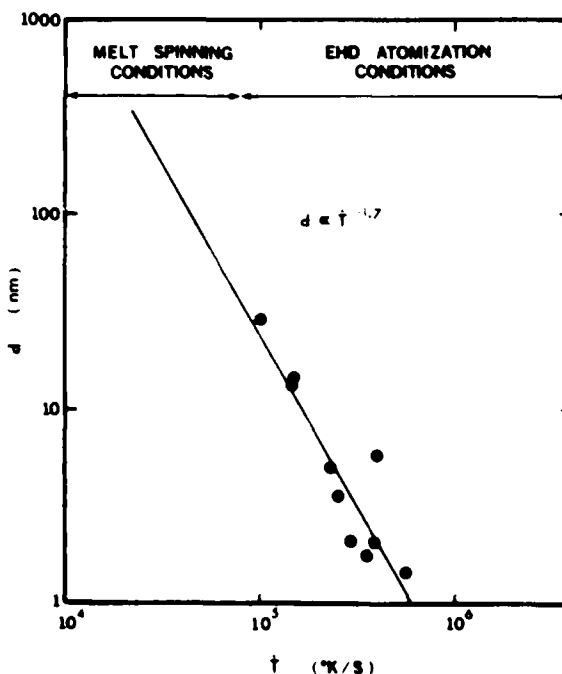


FIG. 8 Experimental dependence of icosahedral grain size (d) on cooling rate \dot{T} , estimated for radiation cooled microparticles ($d \propto \dot{T}^{-1.7}$ is a least-square fit of data)

magnitude higher than what is normally estimated.^{36,37} This makes us believe that nucleation of the icosahedral phase is truly homogeneous.

Metals usually have very high resistance to homogeneous nucleation—most metallic liquids must be undercooled at least to 0.85–0.67 of their absolute melting temperature before the nucleation starts.³⁶ It is the principal factor contributing to the formation of metallic glasses (and also a major stumbling block for microcrystalline models of glass structure). The high resistance of metal melts to homogeneous nucleation can be understood when the topological property of short-range order (SRO) in liquid is contrasted to that in close-packed crystals.^{14,37} First, the SRO of liquid is dominated by the polytetrahedral, or icosahedral, low-energy configuration.^{13–16} Nucleation of three-dimensional close-packed crystals requires essential reconstruction to a tetrahedral/octahedral close-packed structure (dictated by long-range periodicity constraint) at a significant energy cost. Second, the crystal-melt interface energy is a major controlling factor of nucleation resistance.³⁶ This interface energy can be low as a result of the small topological differences between the structure of solid and its undercooled melt.

The low nucleation resistance of the icosahedral phase probably results from the small topological difference between the structures of the phase and its melt. Unfortunately, the exact atomic structure of the icosahedral quasicrystal is still unknown. Nevertheless, quasiperiodically extended icosahedral orientational order implies the presence of extensive SRO.^{8,19} A possible connection between SRO in metallic glasses and icosahedral quasicrystal is also supported when the structure factor of metallic glasses is compared to the diffraction pattern of the icosahedral phase.¹⁹ As expected, among the most intense Bragg peaks are those of the first and second generation of the icosahedral phase where the first generation corresponds to the star of reciprocal lattice vectors, q_0 , pointing to the vertices of an icosahedron, and the second generation is a linear combination of the q_0 's, q' . The position ratio of the peaks for the icosahedral phase is $q'/q_0 = 1, 1.052, 1.701, \text{ and } 2$. The same ratio was found for presumably amorphous diffraction of the smallest Al-Mn particles [see Fig. 3(c)] and is also typical for many metallic glasses.¹⁹

Glass formation is usually possible in systems where crystal nucleation is difficult and the ratio of the glass temperature to the liquidus temperature is relatively high.³⁶ The low nucleation resistance of the icosahedral phase prevents glass formation in this classical manner. The diffraction pattern on Fig. 3(c) can result from nanometer size icosahedral grains formed by nucleation and growth as well as from configurationally frozen liquid (truly glass). In view of this result, it is not clear if the reported Al-Mn glass^{22–24} is indeed the

amorphous structure and not *microquasicrystalline*. In fact, we can speculate on the possibility of existence of class of glass-type material with microquasicrystalline structure. This structure doesn't have the major limitations of previous microcrystalline models: (1) lack of SRO, (2) difficulties of crystal nucleation. Moreover, as was pointed out by Turnbull,³⁷ the same kind of arguments about nucleation may be applied to the formation of a Frank-Kasper phases, in which case, micro-Frank-Kasper-crystallites "glass" will be expected. However, much more work should be done to resolve this issue, especially x-ray and extended x-ray absorption fine structure (EXAF) studies of local atomic order, both for glass-like and quasicrystalline phases.

V. CONCLUSIONS

The study of icosahedral phase formation using submicron droplets of Al-26 wt. % Mn alloy suggests that:

- (1) The icosahedral phase forms by homogeneous nucleation.
- (2) The possible topological similarities between the liquid and icosahedral quasicrystal can explain the lower resistance to nucleation.
- (3) Formation of glass as a configurationally frozen liquid in Al-Mn system is questionable, implying that the reported glass probably has a microquasicrystalline structure.

ACKNOWLEDGMENTS

Gratitude is expressed to our colleagues, W. J. Boettinger, J. W. Cahn, M. J. Kaufman, R. J. Schaefer, and D. Shechtman for helpful discussions and review of the manuscript. It is also a pleasure to thank Professor D. Turnbull, Professor D. Nelson, and Professor S. Moss for valuable comments. Support by the Defense Advanced Research Projects Agency is gratefully acknowledged.

REFERENCES

- ¹D. Shechtman, I. Blech, D. Gratias, and J. W. Cahn, *Phys. Rev. Lett.* **53**, 1951 (1984).
- ²P. A. Bancel and P. A. Heiney, University of Pennsylvania preprint.
- ³P. Ramachandrarao and G. V. S. Sastry, *Pramana* **25**, L225 (1985).
- ⁴G. V. S. Sastry, P. Ramachandrarao, and T. R. Anantharaman, preprint.
- ⁵L. A. Bendersky and F. S. Biancaneello, unpublished research, National Bureau of Standards, Gaithersburg, MD 1985.

- ⁶S. J. Poon, A. J. Drehman, and K. R. Lawless, *Phys. Rev. Lett.* **55**, 2324 (1985).
- ⁷Z. Zhang, H. W. Ye, and K. H. Kuo, *Philos. Mag.* **A52**, L49 (1985).
- ⁸D. Levine and P. J. Steinhardt, *Phys. Rev. Lett.* **53**, 2477 (1984).
- ⁹P. Bak, *Phys. Rev. Lett.* **54**, 1517 (1985).
- ¹⁰V. Elser, *Phys. Rev. Lett.* **54**, 1730 (1985).
- ¹¹M. Duneau and A. Katz, *Phys. Rev. Lett.* **54**, 2688 (1985).
- ¹²P. A. Kalugin, A. Yu Kitaev, and L. C. Levitov, *JETP Lett.* **41**, 145 (1985).
- ¹³C. L. Briant, *Discuss. Faraday Soc.* **61**, 25 (1976).
- ¹⁴F. Spaepen and D. Turnbull, *Rapidly Quenched Metals, Second International Conference*, edited by N. J. Grant and B. C. Giessen (Massachusetts Institute of Technology, Cambridge, MA, 1986), p. 513.
- ¹⁵J. Dixmier and J. F. Sadoc, in *Metallic Glasses* (American Society for Metals, Metals Park, OH, 1978), p. 97.
- ¹⁶F. C. Frank, *Proc. R. Soc. London Ser. A* **215**, 43 (1952).
- ¹⁷F. C. Frank, and J. S. Kasper, *Acta Crystallogr.* **11**, 184 (1958); **12**, 483 (1959).
- ¹⁸D. R. Nelson, *Phys. Rev. B* **28**, 5513 (1983); *J. Non-Cryst. Sol.* **61**, 475 (1984).
- ¹⁹S. Sachdev and D. R. Nelson, *Phys. Rev. B* **32**, 4592 (1985).
- ²⁰V. Elser and C. L. Henley, *Phys. Rev. Lett.* **55**, 2883 (1985).
- ²¹C. L. Henley and V. Elser, *Philos. Mag.* **B53**, 159 (1986).
- ²²D. A. Lilienfeld, M. Nastasi, H. M. Johnson, D. G. Ast, and J. W. Mayer, *Phys. Rev. Lett.* **55**, 1587 (1985).
- ²³L. A. Knapp and D. M. Follstaedt, *Phys. Rev. Lett.* **55**, 1591 (1985).
- ²⁴K. Urban, N. Moser, and H. Kronmüller, *Phys. Status Solidi A* **91**, 411 (1985).
- ²⁵J. Perel, J. F. Maghoney, P. Duwez, and B. E. Kalensher, in *RSP: Principles and Technology II*, edited by R. Mehrabian, B. H. Kear, and M. Cohen (Claitor, Baton Rouge, LA, 1980).
- ²⁶P. A. Bancel, P. A. Heiney, P. W. Stephens, A. I. Goldman, and P. M. Horn, *Phys. Rev. Lett.* **54**, 2422 (1985).
- ²⁷J. W. Cahn, D. Shechtman, and D. Gratias, *J. Mater. Sci.* **1**, 13 (1986).
- ²⁸S. R. Herd and P. Chaudhari, *Phys. Status Solidi A* **26**, 627 (1974).
- ²⁹J. F. Graczyk and P. Chaudhari, *Phys. Status Solidi A* **75**, 593 (1976).
- ³⁰A. Howe, O. L. Krivanek, and M. L. Rudee, *Philos. Mag.* **27**, 235 (1973).
- ³¹M. L. Rudee, *Phys. Status Solidi B* **46**, K1 (1971).
- ³²J. L. Robertson, M. E. Misenheimer, S. C. Moos, and L. Bendersky, submitted to *Acta Metall.*
- ³³L. Bendersky, R. J. Schaefer, F. S. Biancaneello, W. J. Boettinger, M. J. Kaufman, and D. Shechtman, *Scr. Metall.* **19**, 909 (1985).
- ³⁴R. J. Schaefer, L. Bendersky, D. Shechtman, W. J. Boettinger, and F. S. Biancaneello, *Metall. Trans. A.* (to be published).
- ³⁵R. J. Schaefer and L. Bendersky, *Scr. Metall.* **20**, 745 (1986).
- ³⁶D. Turnbull, *Contemp. Phys.* **10**, 473 (1969).
- ³⁷D. Turnbull, in *International Conference on the Theory of the Structures of Non-Crystalline Solids* (North-Holland, Amsterdam, 1985).

An Analysis of the Microstructure of Rapidly Solidified Al-8 Wt Pct Fe Powder

W. J. BOETTINGER, L. BENDERSKY, and J. G. EARLY

Rapidly solidified powders of Al-8 wt pct Fe exhibit four distinct microstructures with increasing particle diameter in the size range of 5 μm to 45 μm : microcellular α -Al; cellular α -Al; α -Al + Al_3Fe eutectic; and Al_3Fe primary intermetallic structure. Small powder particles ($\sim 10 \mu\text{m}$ or less) undercool significantly prior to solidification and typically exhibit a two-zone microcellular-cellular structure in individual powder particles. In the two-zone microstructure, there is a transition from solidification dominated by internal heat flow during recalescence with high growth rates (microcellular) to solidification dominated by external heat flow and slower growth rates (cellular). The origin of the two-zone microstructure from an initially cellular or dendritic structure is interpreted on the basis of growth controlled primarily by solute redistribution. Larger particles experience little or no initial undercooling prior to solidification and do not exhibit the two-zone structure. The larger particles contain cellular, eutectic, or primary intermetallic structures that are consistent with growth rates controlled by heat extraction through the particle surface (external heat flow).

I. INTRODUCTION

ALUMINUM alloys containing ~ 8 wt pct Fe and smaller additions of Ce, Mo, V, or Zr are currently the focus of several high temperature alloy development programs using rapid solidification technology. These programs are an outgrowth of research on Al-Fe binary alloys prepared by splat cooling or surface melting.¹⁻⁴ This research has recently been reviewed by Skinner, Okazaki, and Adam.⁵ The present paper is concerned with the microstructural characterization of atomized powder of Al-8 wt pct Fe and the analysis of the solidification mechanisms which produce these structures.

The phase diagram including metastable phase boundaries has been evaluated by Murray⁶ and is shown in Figure 1. A prominent feature is the metastable phase Al_3Fe and its metastable eutectic with α -Al at $\sim 650^\circ\text{C}$ and ~ 3.2 wt pct Fe. The extended α -Al liquidus and solidus as well as the T_0 curve for the partitionless solidification of α -Al has also been estimated. One can see that for Al-8 wt pct Fe, the solidification of several metastable structures is thermodynamically possible depending on the transformation temperature.

In fact, hypereutectic aluminum-iron alloys are well known to exhibit a wide range of microstructures depending on the solidification velocity. Alloys with compositions up to 4 wt pct Fe were studied by Adam and Hogan,⁷ and alloys up to 6.1 wt pct Fe were studied by Hughes and Jones⁸ using directional solidification. This work showed that for alloys above 3 wt pct Fe three distinct microstructures were observed for solidification velocities in the range between 0.1 cm/s and 1 cm/s. Near 0.1 cm/s the structure consists of primary intermetallic faceted dendrites of Al_3Fe with a eutectic of α -Al and Al_3Fe between the primary dendrites. Near 0.5 cm/s the structure consists of a fully eutectic structure of α -Al and Al_3Fe . Near 1 cm/s the structure consists

of cells of α -Al with a eutectic of α -Al + Al_3Fe between the cells. The precise transition velocities depend on composition and are understood by an analysis of the asymmetric coupled zone for this alloy.⁹ Similar microstructural variations are found in the present work on atomized powder.

When a liquid alloy is broken up into a large number of fine droplets, as occurs in atomization, the most potent nucleation sites can become dispersed such that large liquid undercoolings below the equilibrium liquidus may be achieved prior to nucleation. Nucleation studies performed at slow cooling rates by the droplet-emulsion technique by Perepezko, LeBeau, Mueller, and Hildeman⁹ on Al-Fe alloys show the possibility of large liquid undercoolings prior to solidification. Al-5 wt pct Fe powders with diameters of 10 μm undercooled to $\sim 520^\circ\text{C}$ (260 K below the Al_3Fe liquidus and 123 K below the α -Al liquidus) prior to solidification. Their results also show that in Al-9 wt pct Fe, nucleation of Al_3Fe occurs at temperatures between the

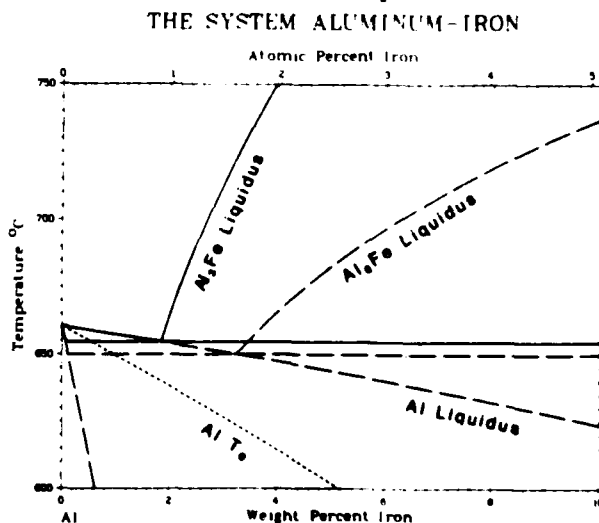


Fig. 1—Al-rich portion of the Al-Fe phase diagram⁶ showing stable (Al-Al₃Fe) diagram and metastable (Al-Al₃Fe) diagram. The extended α -Al liquidus and solidus as well as the T_0 curve for partitionless solidification of α -Al are also shown. The α -Al solvus curves are omitted for clarity.

W. J. BOETTINGER and J. G. EARLY are Metallurgists with the Metallurgy Division, National Bureau of Standards, Gaithersburg, MD 20899. L. BENDERSKY is with the Center for Materials Science, The Johns Hopkins University, Baltimore, MD 21218 and is also a Guest Worker at the National Bureau of Standards.

Manuscript submitted May 13, 1985.

Al₃Fe liquidus and the α -Al liquidus. However, upon further cooling the nucleation of a second phase, α -Al, does not occur until 565 °C.

When nucleation does occur in an undercooled droplet, the initial solidification rate is extremely rapid. This initial rate depends strongly on the solid-liquid interface morphology. It is convenient to define a dimensionless undercooling $\Delta\theta = \Delta T/(L/C)$ where ΔT is the initial undercooling below the relevant liquidus temperature, L is the latent heat per unit volume, and C is the liquid heat capacity per unit volume. For $\Delta\theta < 1$, solidification can occur in one of three different morphologies for the case of a single nucleation event on the droplet surface as shown in Figure 2. In Figure 2(a), a dendritic interface moves at a near constant velocity across the entire particle to form a mixture of liquid and solid at the end of recalescence. The interdendritic regions solidify later by removal of latent heat to the powder exterior usually at a much slower rate. In Figure 2(b) a smooth interface moves partially across the powder to produce a particle which is composed of two zones, one solid and one liquid at the end of recalescence. Solidification is again finished by removal of latent heat to the powder exterior usually at a much slower rate to produce the coarse segregated structure shown on the right. In each case the fraction of the powder which is solid at the end of recalescence is equal to $\Delta\theta$.*

*The volume fraction solid at the end of recalescence is $\Delta\theta$ when the heat lost to the powder exterior is zero during recalescence. Furthermore, for alloys the relationship between fraction solid and $\Delta\theta$ is essentially correct but will depend on the degree of segregation in the solid.

Figure 2(a) the microstructure is relatively uniform across the powder dimensions. In the case shown in Figure 2(b) the internal heat flow and changes in the liquid-solid interface temperature, velocity, and shape combine to produce a

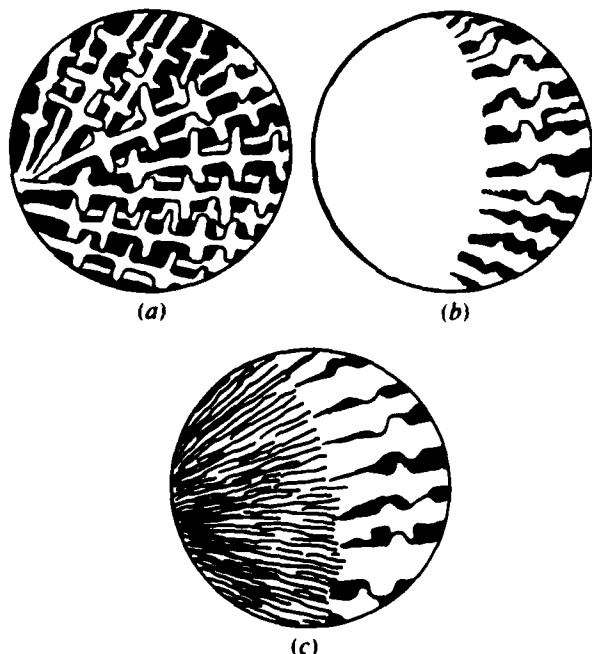


Fig. 2—Schematic representation of the solidification of initially undercooled liquid droplets for nucleation on the surface when the initial interface is (a) dendritic, (b) smooth, and (c) cellular.

strongly time-dependent solidification process and a microstructure which varies across the droplet dimensions.

This latter situation has been analyzed in detail by Levi and Mehrabian.¹⁰ Using numerical techniques they have shown that under a broad range of conditions, external cooling of atomized powder is incapable of suppressing this recalescence. In a companion paper,¹¹ they demonstrated that Al-Si and Al-Cu submicron powders exhibit two microstructural zones as depicted in Figure 2(b): one dominated by internal heat flow and hence high solidification rate, and one dominated by external heat flow and hence slower solidification rates. Similar results were calculated for solidification of a thin melt in contact with a cold substrate by Clyne.¹²

The occurrence of two microstructural zones is frequently observed in rapidly solidified powders and melt spun ribbons. However, the solidification of the first zone does not usually occur with a smooth interface for Al-8 wt pct Fe.^{1,9} This case is shown in Figure 2(c), where the first zone solidifies with a fine cellular interface. At the end of recalescence the volume fraction of the powder which contains the cellular structure is $\Delta T/(L'/C)$ where L' is a fraction of the ordinary latent heat. This fraction is equal to the volume fraction solid within the cellular structure at the end of recalescence. The coarser structure to the right again forms after recalescence is complete. The present paper also focuses on understanding the reasons for this morphology in contrast to those shown in Figures 2(a) and 2(b).

II. EXPERIMENTAL PROCEDURE

The powder was atomized by Homogeneous Metals, Clayville, NY,* by upward ejection of molten alloy using

*The name of the supplier is provided for completeness only and does not constitute a product endorsement by the National Bureau of Standards.

high pressure Ar through a SiO₂ tube into an initially evacuated (3 Pa (3×10^{-5} atm)) collection chamber. However, final chamber pressures are typically 3×10^4 Pa (0.3 atm). The Al-8 wt pct Fe starting alloy was made from 99.99 pct pure Al and 99.9 pct pure Fe components. The size analysis of the powders is shown in Figure 3. Four size fractions, 5 to 10 μ m, 10 to 20 μ m, 20 to 30 μ m, and 30 to 45 μ m, were examined by optical and transmission electron microscopy. Small samples (3 mm diameter \times 0.5 mm thick)

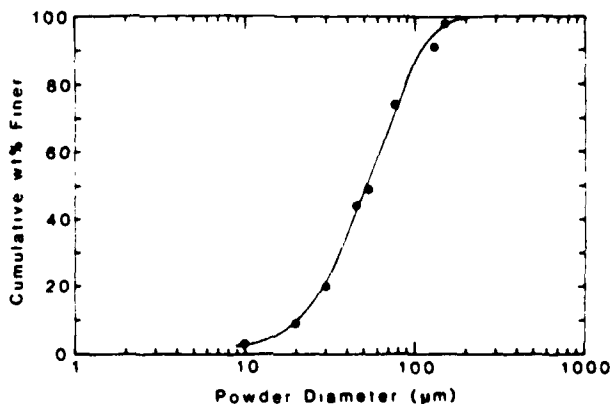


Fig. 3—Size analysis of the as-received Al-8 wt pct Fe powder

were cold pressed in a tungsten carbide die following a technique developed by Shechtman and Gutmanis.¹³ For optical microscopy, these samples were prepared by standard metallographic technique and etched with Keller's reagent. For transmission electron microscopy, these samples were prepared by twin jet electropolishing in an electrolyte of 950 ml methanol, 50 ml HClO₄, and 15 ml HNO₃ at -30 °C.

III. RESULTS

Four general types of microstructure were observed in the powder particles: microcellular α -Al, cellular α -Al, fully eutectic structure of α -Al and Al₆Fe, and primary intermetallic Al₃Fe structure. The occurrence of these structures is ranked by increasing particle size. Generally the microcellular structure is seen only in very small particles and the primary intermetallic structure is seen only in large particles. First, the details of the four microstructures will be described and second, the abundance of these structures as a function of powder size will be given.

Microcellular and Cellular Structures. Figure 4 is a TEM micrograph of a thin foil of the entire cross-section of a powder particle. This micrograph demonstrates several features typical of the atomized powder microstructures in the size range between 5 and 20 μ m. The particle consists primarily of fcc α -Al with a single crystallographic orientation. Nucleation appears to have occurred at a single site on the surface of the particle on the left and the solidification front has passed from left to right. The microstructure near the point of nucleation is extremely fine and is termed microcellular in the present paper. The microstructure on the right is a more usual coarse cellular structure of α -Al. A few powder particles consist of several grains or colonies of the microcellular/cellular two-zone structure which indicates multiple nucleation.

The microcellular structure contains a very fine segregation pattern with cell spacings ranging between 25 and 100 nm but with a typical spacing of 50 nm. The intercellular regions contain fine Fe-rich particles whose identity is uncertain and unimportant to the analysis presented in this paper. Electron diffraction patterns show rings from the fine particles which cannot be indexed as Al₃Fe or Al₆Fe. Most

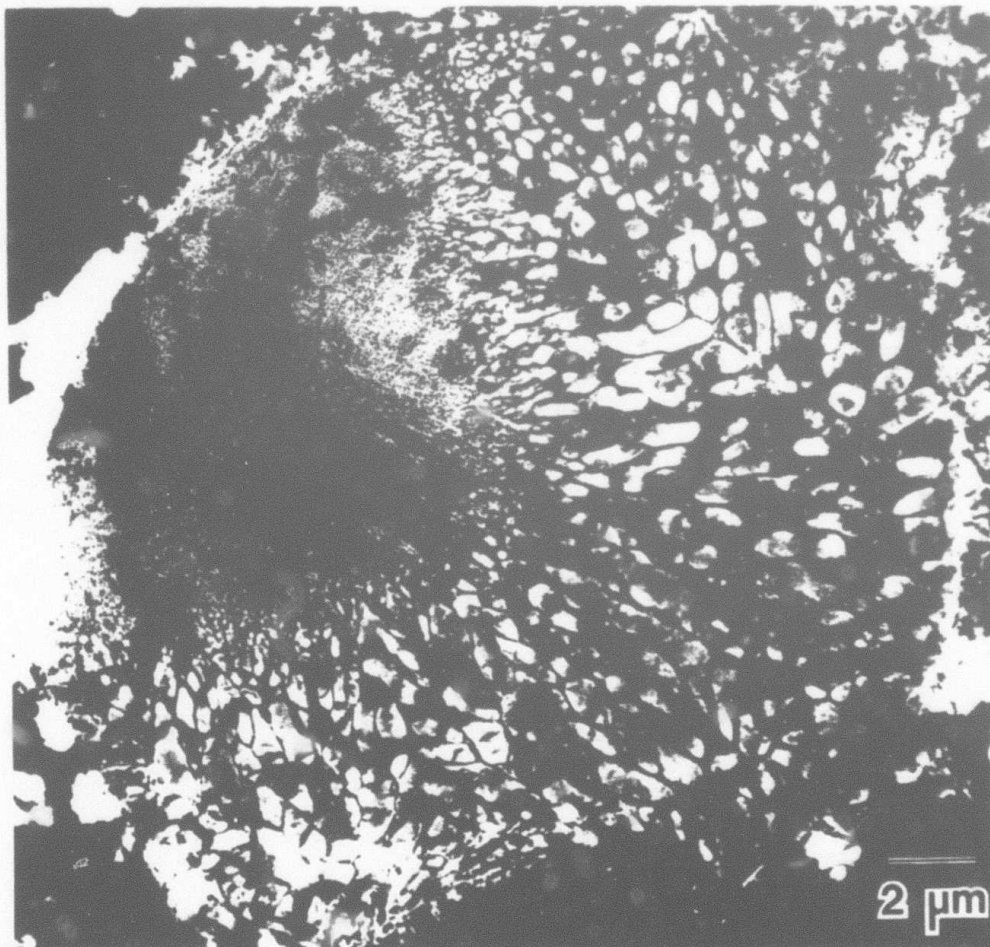


Fig. 4—TEM micrograph of a cross section through a rapidly solidified Al-8 wt pct Fe powder particle. A single nucleation site (left) initiates solidification with a high interface velocity to produce a fine cellular structure. Recalescence slows the interface velocity to produce the coarser cellular structure at the right. This structure is very common in powders $\sim 10 \mu$ m in diameter.

powder particles below $5 \mu\text{m}$ in diameter consist entirely of this microcellular structure as shown in Figure 5. Nucleation occurs on the powder surface, but due to the cross section shown which does not contain the nucleation site, the structure seems to radiate from the interior of the particle. The large light and dark regions of the particle suggest some slight misorientations due to the presence of subgrains within the "single grain" of $\alpha\text{-Al}$. The presence of the microcellular structure implies that the solubility extension of Fe in fcc $\alpha\text{-Al}$ is far less than 8 wt pct Fe in these powders. Identical microcellular structures have been observed by several other investigators in Al-8 wt pct Fe; viz., Jones,¹ Jacobs, Dogett, and Stowell,² and for alloys containing Mo, by Adam.¹⁴ Adam called these structures microeutectic and claimed that the intercellular regions were amorphous.

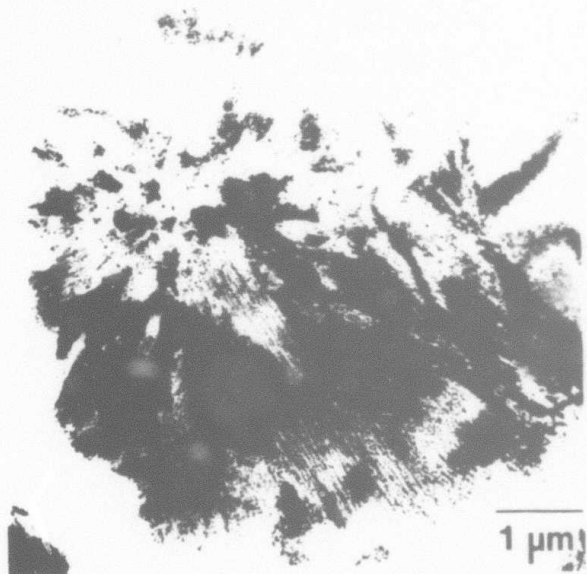


Fig. 5—TEM micrograph of a cross section through a small powder particle ($\sim 5 \mu\text{m}$) which solidified with the microcellular structure only.

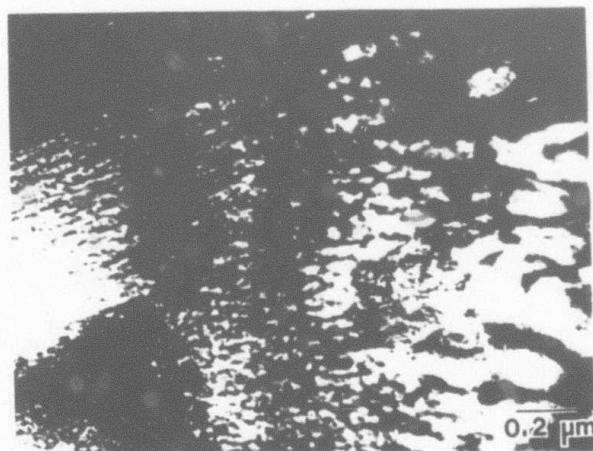
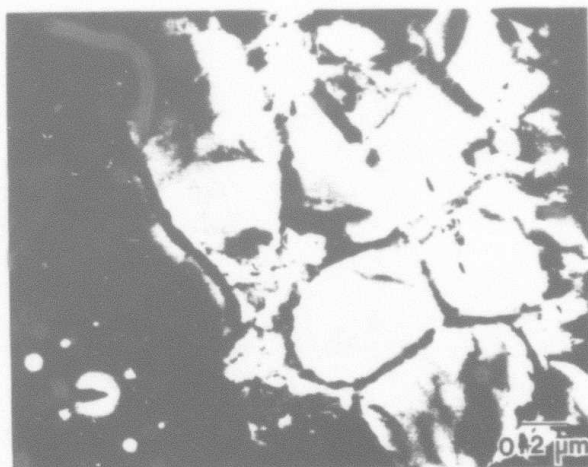
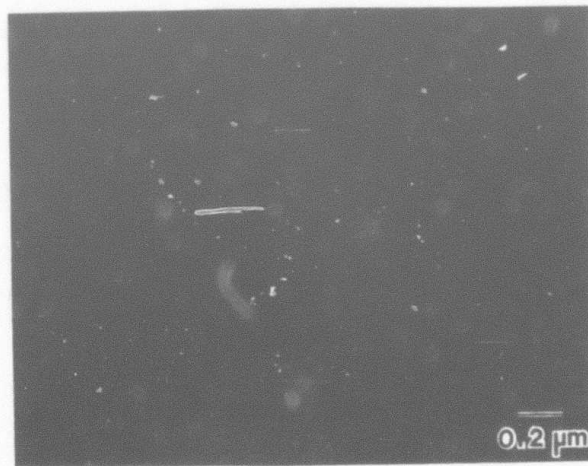


Fig. 6—Transition region between fine microcellular and coarse cellular structures.

Figure 6 shows a high magnification view of the rather sharp transition region from the microcellular to the cellular structure. The plane of the thin foil section does not exactly contain the growth direction and hence the cells appear discontinuous in the growth direction. These coarser cellular structures have spacings between 100 nm and $1 \mu\text{m}$ but with a typical spacing of $0.5 \mu\text{m}$. Figures 7(a) and 7(b) are a bright field/dark field pair of TEM micrographs which show that the intercellular regions consist of many small randomly oriented particles with a characteristic diffraction pattern shown in the inset. Similar ring patterns are found for the intercellular regions of the microcellular structure. Due to their extremely small sizes these particles may be the result of solid state decomposition after solidification. Dark-field micrographs (not shown) using reflections from the $\alpha\text{-Al}$ cells show that the intercellular regions contain no $\alpha\text{-Al}$ with the same orientation as the cells. Hence the small precipitates do not form by decomposition of Fe supersaturated $\alpha\text{-Al}$. A more likely possibility is that the cell



(a)



(b)

Fig. 7—Cellular structure of Al-8 wt pct Fe rapidly solidified powder showing nature of intercellular microconstituent. (a) Bright field. (b) Dark field of precipitate.

walls solidified as another phase which subsequently decomposed into the fine precipitates. Due to the randomness of orientations of the small particles it is probable that the original intercellular phase was amorphous Al-Fe enriched in Fe. Some of the coarsest cellular structures contain Al_3Fe in the intercellular regions.

Eutectic Structure of α -Al and Al_3Fe . Figure 8 is a TEM micrograph typical of powder particles ~ 20 to $30 \mu m$ in diameter. The particle has solidified as a eutectic consisting of rods of Al_3Fe in a matrix of α -Al. In the particle the eutectic spacings range between 90 and 180 nm. No sharp boundary delineating a two-zone microstructure of fine and coarse eutectic is seen. This result suggests that recalescence was not a significant factor in the solidification of this particle. The eutectic is also found in some intercellular regions as shown in Figure 9.

Primary Intermetallic Al_3Fe . Many powders in the 30 to $45 \mu m$ size fraction contain large particles of Al_3Fe which grow from the liquid as the first or primary constituent. These particles often exhibit a blade or plate shape with the longest dimension between 1 and $20 \mu m$. Figure 10 shows a typical region with primary intermetallics which grow in a complex intersecting pattern. The regions between the Al_3Fe particles are α -Al. The α -Al exhibits a fine subgrain structure. Occasionally an additional primary phase was observed. This phase exhibits a hexagonal-like morphology, with a corresponding 6-fold SAD pattern. However, convergent beam diffraction suggests 3-fold symmetry.

Dependence of Microstructure on Powder Size. Figures 11 and 12 show optical micrographs of the cold pressed powders from the 5 to $10 \mu m$ and 30 to $45 \mu m$ size fractions. Unetched regions are very common in Figure 11 and correspond to the microcellular structure observed in TEM micrographs. Particles containing the cellular structure can also be seen, but cellular and eutectic structures can not usually be distinguished in the optical micrographs. A few powder particles contain blades or plates of the faceted

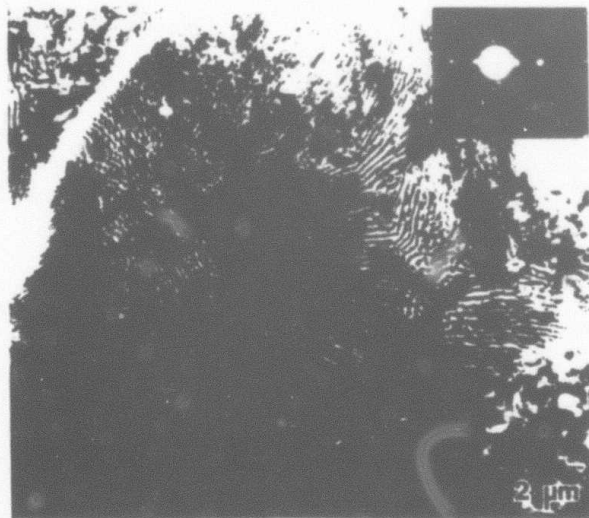


Fig. 8—Fully eutectic structure typical of that seen in 20 to $30 \mu m$ diameter powder particles. The SADP identifies the metastable phase Al_3Fe which occurs as rods in a matrix of α -Al to form the eutectic structure.

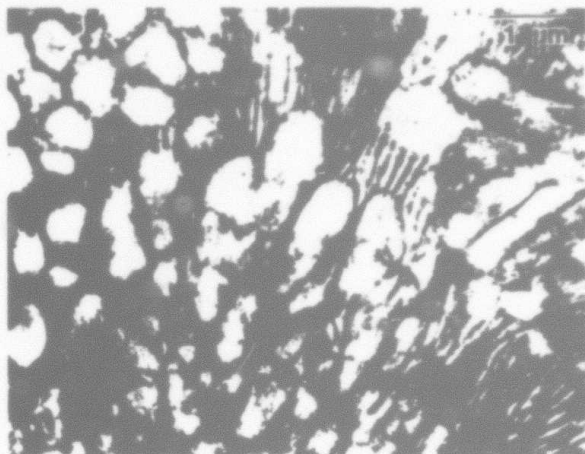


Fig. 9—Cellular structure of α -Al with intercellular regions containing eutectic of α -Al and Al_3Fe .

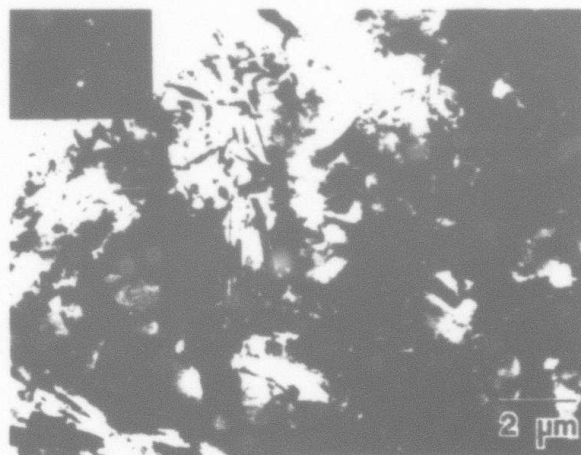


Fig. 10—Complex structure typical of large powder particles ($>30 \mu m$) which contain blades of Al_3Fe which form directly from the melt.

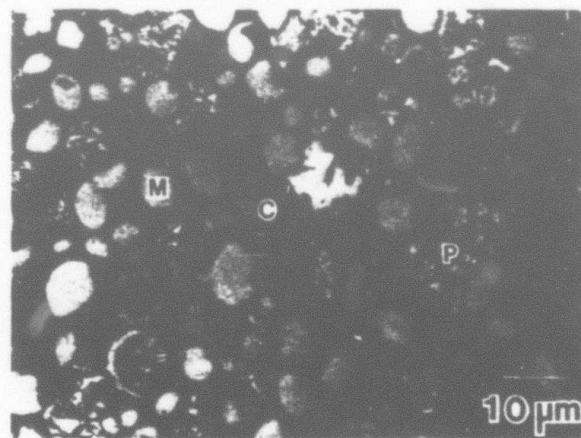


Fig. 11—Optical micrograph of a cold pressed sample of 5 to $10 \mu m$ Al-8 wt pct Fe powder. Note the variation in microstructure within individual powder particles as well as the variation among particles. M = microcellular, C = cellular, and P = primary intermetallic.

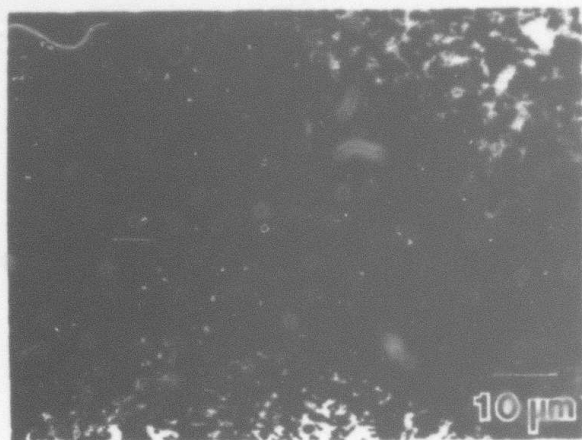


Fig. 12—Optical micrograph of a cold pressed sample of 30 to 45 μm Al-8 wt pct Fe powder. Note the large number of particles containing primary intermetallic crystals of Al_3Fe .

primary intermetallic phase. Powders containing these primary intermetallic phases are much more common in Figure 12.

To obtain information about the relative abundance of the four microstructures as a function of powder size, the volume fractions of (a) the microcellular, (b) the combined cellular and eutectic, and (c) the primary intermetallic structure were estimated from micrographs of the cold pressed powders using the linear intercept method. These data for the various size fractions are given in Figure 13. Also pos-

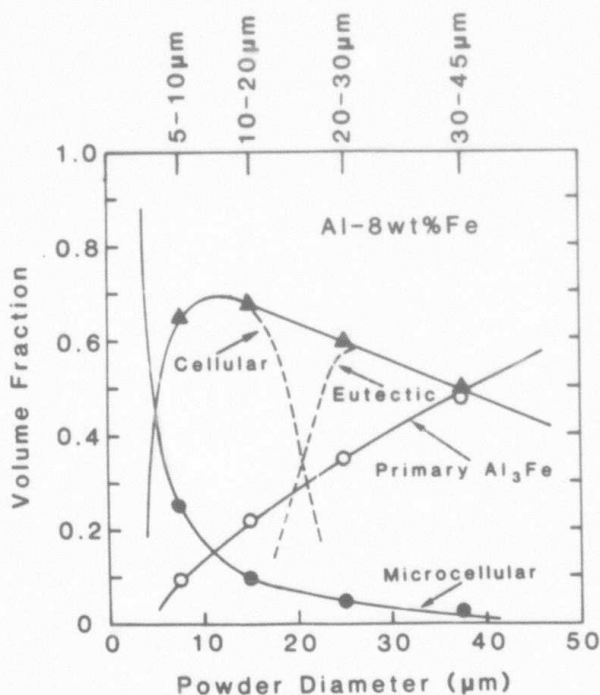


Fig. 13—Volume fraction of the microcellular, combined cellular and eutectic, and primary intermetallic structures as a function of powder diameter. Possible separate curves for the cellular and eutectic structures are shown dashed.

sible separate curves for the cellular and eutectic structures are shown dashed, which when summed equal the measured data. The curve for the microcellular structure includes the result from electron microscopy that most particles below 5 μm diameter are completely microcellular. It must be remembered that individual powders of the same size may contain varying amounts of microcellular structure. It appears that the cellular and eutectic structures are most common in 10 and 25 μm diameter powders, respectively. The primary intermetallic structure is most common in powders larger than 40 μm .

IV. DISCUSSION

In the larger diameter powder particles the absence of a two-zone structure and the relative coarseness of the microstructures indicate that the degree of undercooling prior to solidification *does not contribute* significantly to the growth rate. The absence of large initial undercooling is most likely due to the presence of a concentration of potent catalytic sites for nucleation within the bulk alloy which do not become isolated into a minor fraction of the powder particles unless the particle size is less than $\sim 10 \mu\text{m}$. This agrees quite well with the experimental observation of a large increase in the undercooling capacity of Al-Fe alloys with powder size refinement to the 10 μm size range.⁹ For the small powders nucleation occurs on the powder surface and is therefore also heterogeneous albeit on much less potent catalytic sites. In these particles the initial undercooling *does contribute* significantly to the growth rate. The discussion will therefore be divided into two sections: the first deals with the large particles where the solidification velocity is controlled by extraction of heat to the powder exterior and where the microstructures formed are cellular, eutectic, or primary intermetallic. The second section deals with the small particles where the solidification velocity is a function of the initial undercooling and the two-zone microcellular-cellular structures are observed.

A. Solidification with No Initial Undercooling

A simple model for powder solidification will now be proposed to guide the interpretation of the present results. To avoid the geometrical and calculational complexities of the spherical solidification geometry, a spherical powder particle of diameter d will be approximated by a cylinder of diameter d and height d . From a thermal viewpoint, solidification will occur with a planar interface moving at velocity V_s (for external) from one cylinder face to the other. Prior to nucleation the temperature difference within a powder particle is small if the Biot number, $\text{Bi} = hd/k_L \ll 1$, where h is the heat transfer coefficient and k_L is the thermal conductivity of the liquid alloy. If the operating gas pressure in the atomization chamber is above $2 \times 10^3 \text{ Pa}$ ($2 \times 10^{-2} \text{ atm}$), the thermal conductivity of the argon gas, k_{gas} , is at least 75 pct of the conductivity at $1 \times 10^5 \text{ Pa}$ (1 atm).¹⁵ Because the relative velocity of the particle and the gas is small, the heat transfer is primarily by conduction and h (for a spherical particle) is given by

$$h = 2k_{\text{gas}}/d \quad [1]$$

Hence $\text{Bi} = 2k_{\text{gas}}/k_L \approx 10^{-4}$. (Values of the various thermophysical parameters used are given in the Appendix.)

After nucleation, release of latent heat of fusion will be effectively spread throughout the entire powder particle if $Vd/\alpha \ll 1$ where α is the thermal diffusivity for the liquid alloy. For a 20 μm diameter particle this condition is satisfied if $V \ll 170$ cm/s.

For an isothermal powder, a simple heat balance during solidification gives the solidification velocity, V_s , controlled by external heat extraction as

$$V_s = \frac{6h\Delta T_s}{L} \quad [2]$$

where ΔT_s is the temperature difference between the sample and the cooling gas.* The predictions of this expression

*For the same assumptions used to calculate V_s , the cooling rate of the liquid prior to solidification can be expressed by $6h\Delta T_s/Cd$ or LV_s/Cd .

agree reasonably well with the "minimum velocities" given by Levi and Mehrabian in their Table IV using spherical geometry.¹⁰ For the present case of conductive cooling V_s is given by

$$V_s = \frac{12k_{gas}\Delta T_s}{Ld} \quad [3]$$

Table I gives values of h and V_s for various diameter powder particles using $k_{gas} = 1.34 \times 10^{-4}$ J/cm s K, and $\Delta T_s = 600$ K.

The observed microstructures in the large powders are consistent with the effect of powder size on V_s . From the experiments of Hughes and Jones,⁸ the microstructure of Al-6 wt pct Fe changes from a primary Al₃Fe intermetallic structure to a fully eutectic structure of α -Al + Al₃Fe and finally to a cellular structure of α -Al in the range of growth velocity between 0.1 and 1 cm/s. Slightly higher transition velocities would be expected for Al-8 wt pct Fe. An identical change in microstructure is observed for Al-8 wt pct Fe powders with diameters between 50 and 10 μm where the estimated growth rate for initially nonundercooled powders also changes from ~ 0.2 to 1 cm/s (see Table I). Additionally, Hughes and Jones⁸ measured the λ^2V constant which relates the eutectic spacing, λ , to the growth rate for the α -Al + Al₃Fe eutectic as a function of iron content. Extrapolating their results to Al-8 wt pct Fe gives a λ^2V constant of $\sim 3.8 \times 10^{-11}$ cm²/s. The range of eutectic spacings observed in the present experiments is 90 to 180 nm in powders with diameters between 20 and 40 μm . The spacings indicate growth rates between 0.5 and 0.1 cm/s. This is in general agreement with the fact that eutectic structures are most common in powder between 20 and 40 μm in diameter. Hence the occurrence of the cellular, eutectic, and primary intermetallic structures in the

Table I. Estimated Heat Transfer Coefficients and Growth Rate for Powders with No Initial Undercooling

d (μm)	h (J/cm ² s K)	V_s (cm/s)
5	0.54	2.0
10	0.27	1.0
20	0.13	0.50
30	0.09	0.33
40	0.07	0.25
50	0.05	0.20

larger size particles is consistent with a rate of growth controlled by extraction of heat through the powder exterior.

The absence of *initial* undercooling does not imply that these particles are not undercooled during solidification. During cooling from the liquid state one envisions a hypothetical situation where Al₃Fe, Al₃Fe, and α -Al may all nucleate. However, competitive growth of these phases at the growth velocity imposed by the external heat extraction rate will determine the dominant microstructure. The temperature of the particle during this solidification will be close to the interface temperature for the growth of the dominant microstructure. Later in this paper the temperature of the interface for cellular solidification of α -Al will be obtained. Analysis of the interface temperature for eutectic and for primary intermetallic solidification has been performed by Hughes and Jones.⁸

B. Solidification with Initial Undercooling

Levi and Mehrabian¹⁰ have calculated the interface position and velocity for an initially undercooled powder particle subject to external cooling where nucleation occurs on the surface. They assumed that a smooth interface was morphologically stable and governed by an interface kinetic law involving only interface attachment. In the undercooled powders in the present experiments the interface is clearly cellular and a different approach is necessary to estimate the effect of initial undercooling on the growth rate. It will be shown below that the position and velocity of the cellular interface can be modeled using a kinetic law for the interface involving only solute redistribution and a thermal balance for the entire powder using an effective latent heat L' .

Isolated Growth of an Al-8 Wt Pct Fe Dendrite. To analyze the kinetics of alloy cellular or dendritic growth of α -Al into an undercooled melt, a recent theory by Lipton, Glicksman, and Kurz¹⁶ will be applied. This theory predicts the growth rate of an isolated dendrite tip as a function of undercooling, ΔT , for various alloy compositions, C_0 , assuming local equilibrium at the liquid-solid interface. The theory includes the effects of solute redistribution, latent heat removal, and interface curvature and uses the concept of marginal stability to determine the operating condition at the tip. It thus spans the range from dendritic growth in a pure material where heat flow dominates to dendritic growth in a concentrated alloy where solute redistribution dominates. The undercooling ΔT is the difference between the α -Al liquidus temperature for the bulk alloy composition and the temperature of the liquid far from the dendrite tip (the bath or nucleation temperature). In the theory, the undercooling, ΔT , is the sum of three parts: the thermal undercooling, ΔT_t , the solute undercooling, ΔT_s , and the curvature undercooling, ΔT_c . The term ΔT_t is the temperature difference between the dendrite tip and the liquid far from the dendrite. The term ΔT_s is the difference between the liquidus temperatures for the bulk alloy composition and the composition of the liquid at the dendrite tip. The term ΔT_c is the Gibbs-Thomson depression of the liquidus temperature due to the curvature of the dendrite tip.

The assumption of local equilibrium must be abandoned at high solidification rate. However, because the interface partition coefficient k is thought to be close to the equilibrium value as long as the growth rate is much less than

~500 cm/s,¹⁷ the theory is likely accurate to ~50 cm/s. Above this velocity nonequilibrium effects can be introduced into the theory in a continuous manner.

The results of the local equilibrium theory using parameters listed in the Appendix are shown in Figure 14 for 0, 4, and 8 wt pct Fe where tip growth rate, V , is plotted against initial undercooling ΔT . The effect of the high solute content and low equilibrium partition coefficient for Al-8 wt pct Fe is dramatic. For fixed undercooling* the growth

*Often the nucleation temperature of alloys under fixed surface nucleation conditions parallels the liquidus.¹⁸ So comparing the growth rates of alloys at fixed undercooling is more than a mathematical convenience.

rate of Al-8 wt pct Fe dendrites is more than two orders of magnitude slower than pure Al dendrites. In fact, the growth of Al-8 wt pct Fe can for all practical purposes be considered solution growth; *i.e.*, the growth rate is determined by solute redistribution, not heat dissipation, at the dendrite tip. This conclusion is supported by two aspects of the calculations. First, the growth rates for Al-4 and 8 wt pct Fe do not change significantly in the range of undercoolings shown if the calculation is performed for a latent heat of zero. Second, the dendrite tip temperatures for the alloys differ from the temperature far from the interface by less than 2 pct of the bath undercooling, *i.e.*, $\Delta T_i < 0.02 \Delta T$.

For Al-8 wt pct Fe the relationship between ΔT and V can be fit in the range shown by

$$V = 1.49 \times 10^{-4} \Delta T^{2.84} \quad [4]$$

for V and ΔT in cm/s and K, respectively. Because ΔT_i is small in this case, the bath undercooling or the dendrite tip undercooling can be used interchangeably in Eq. [4] to determine the growth velocity, V . As will be seen below, this interchangeability is the key feature which permits the interpretation of the two-zone cellular structures observed in the

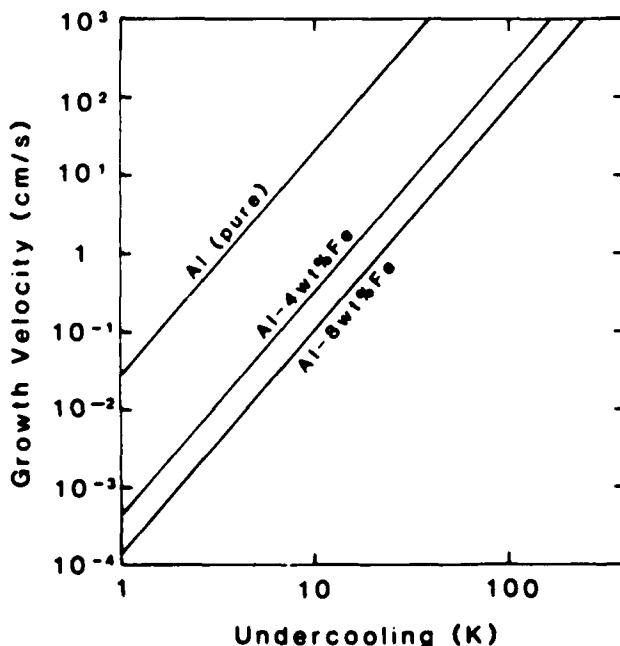


Fig. 14—Calculated dendritic growth rate of pure Al, Al-4 wt pct Fe, and Al-8 wt pct Fe as a function of bath undercooling below the liquidus temperature using the theory of Lipton, Glicksman, and Kurz.¹⁸

present experiments. In general, solute redistribution will dominate in determining the dendritic growth rate whenever the bath undercooling is smaller than the alloy freezing range, $m(k-1)C_0/k$ where m is the liquidus slope.¹⁹ The freezing range for α -Al at the Al-8 wt pct Fe composition is ~750 K.

Nonisolated Dendrites. Under conditions where the growth rate of an isolated dendrite is dominated by solute redistribution, it seems reasonable to assume that the primary spacing of an array of dendrites or cells should also be determined by solute redistribution. If the primary spacing is set at a spacing where the solute fields of adjacent dendrite tips overlap slightly, the thermal fields from adjacent tips will overlap significantly. This is due to the fact that the thermal diffusivity α is four orders of magnitude larger than the solute diffusivity D . When the growth rate of dendrite is dominated by thermal effects (*i.e.*, for small freezing range alloys), the primary spacing is likely set such that neither the thermal nor the solute fields will overlap significantly.

When the thermal fields from adjacent dendrite tips overlap significantly, the motion of an advancing array of dendrite or cellular tips can be modeled as an instantaneously isothermal smooth surface which emits an effective latent heat L' . The temperature of this surface as a function of velocity is given by the kinetic law for an isolated dendrite (Eq. [4]). The divorce of the thermal and solute problems is valid only when the growth rate of an isolated dendrite is dominated by solute redistribution. This approach has recently been used to model equiaxed dendritic growth by Rappaz *et al.*²⁰ A similar method can be used for eutectic growth in an initially undercooled alloy where obviously redistribution of solute dominates the relationship between interface undercooling and growth rate. In this case a different form of Eq. [4] would be used, however.

The latent heat emitted by this effective interface L' will be a fraction of the normal latent heat, governed by the volume fraction solid in the cellular or dendritic array. It is not clear at the present time exactly what factors determine the volume fraction in the cellular or dendrite array. In the limit where the growth rate is determined purely by redistribution of solute, the volume fraction solid in the cellular array is the dimensionless supersaturation (see Reference 16). This is nearly equivalent to using the level rule (conservation of solute) at the temperature of the cell tips to determine the fraction of α -Al. For $\Delta T = 50$ K, the dimensionless supersaturation is ~0.5. However, during recalescence in the microcellular zone, the volume fraction may change. Due to these complexities, the volume fraction for the present analysis is estimated as ~0.7 from the fraction of α -Al in the microcellular region of the micrograph shown in Figure 6. Hence $L' = 0.7L$.

The separation of the thermal and solute problems permits an understanding of how a two-zone microstructure can occur in an undercooled particle when the initial growth is cellular or dendritic. Two-zone structures develop when the latent heat from a freezing interface raises the temperature of the powder in such a way as to diminish the growth rate. For thermally controlled dendritic growth, the thermal field in front of a dendritic array is confined to the proximity of each dendrite tip and the growth rate is constant across a powder particle. For solute controlled growth the thermal field in front of a dendritic array has a characteristic dimension of the entire array. This causes the latent heat to spread

throughout the powder particle and diminish the growth velocity causing a two-zone microstructure.

Powder Solidification. Using the same simplifying geometry and assumptions to model powder solidification as above, the solidification velocity V , of an initially undercooled powder during recalescence with no external heat extraction can now be obtained simply. A heat balance will give the position of the interface x measured from the nucleating cylinder face as a function of the particle temperature T and nucleation temperature T_N as

$$x/d = C(T - T_N)/L'. \quad [5]$$

Using the kinetic law Eq. [4] in a general form

$$V = \mu_n(T_L - T)^n, \quad [6]$$

where T_L is the alloy liquidus temperature, the growth rate V_r can be written as

$$V_r = V_n \left(1 - \frac{1}{\Delta\theta'} \cdot \frac{x}{d} \right)^n \quad [7]$$

where $\Delta\theta' = (T_L - T_N)C/L'$, and V_n is the initial growth rate given by

$$V_n = \mu_n(T_L - T_N)^n. \quad [8]$$

When $Vd/\alpha > 1$ the assumption of an isothermal sample is invalid and the interface will be subject to a local recalescence which will slow growth more quickly as shown by Levi and Mehrabian.¹⁰ For a 10 μm particle, this effect is important when $V > 340$ cm/s.

Figure 15 shows the predicted velocity vs distance solidified using Eqs. [3] and [7] for a 10 μm diameter particle of Al-8 wt pct Fe freezing as α -Al. These velocities are thought to represent the situation which occurred during the solidification of the powder particle shown in Figure 4. The curve V_r would approximate the velocity during recalescence after which a transition to the line V_e would occur. Note the volume fraction of microcellular structure in the entire particle is $\sim 1/3$ and corresponds to the choice of $\Delta\theta' = 1/3$ or a nucleation temperature $(1/3)(L'/C)$ or 85 K below the α -Al liquidus. Note that $V_n = 45$ cm/s from Figure 14 and $V_e = 1$ cm/s from Eq. [8] and Table I. Due to the large decrease in the growth rate as a function of x/d , the cell spacing increases dramatically across the powder. The Lipton-Glicksman-Kurz theory predicts the tip radius of a growing dendrite. For a velocity of 10 cm/s typical of the microcellular zone, the predicted radius is 45 nm. For a velocity of 1 cm/s typical of the cellular zone, the predicted radius is 0.2 μm . These radii compare quite favorably with the cell spacings observed in the microcellular and cellular zones. This comparison is based on the assumption that cell spacings should scale with the tip radius.

Solute Trapping. The absence of a microsegregation-free zone of α -Al in the first region of powder particles to solidify is worthy of note. In fact, except for the work of Jacobs, Doggett, and Stowell,⁴ microsegregation-free structures have not been observed in Al-8 wt pct Fe produced by any rapid solidification technique. For growth into an undercooled melt, the only mechanism by which microsegregation-free structures are produced is partitionless solidification.¹⁷ The precise conditions required for partitionless solidification are not fully understood. A necessary condition is a liquid-solid interface temperature

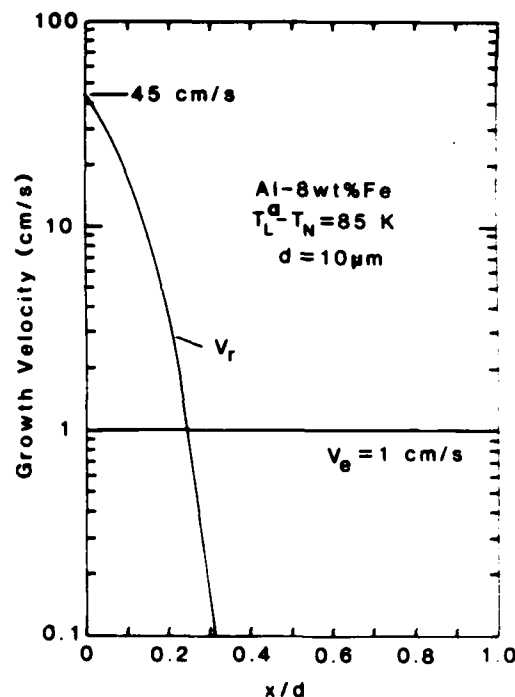


Fig. 15—Estimated growth velocity vs fractional distance across an initially undercooled powder particle. The curve V_r is the velocity for solidification of α -Al cellular structure during recalescence with no external heat extraction. The line V_e is the velocity established by the external heat extraction. The initial undercooling is ~ 85 K below the α -Al liquidus and produces an initial growth rate of 45 cm/s. The heat transfer coefficient is $0.27 \text{ J/cm}^2 \text{ s K}$ and produces a growth rate of 1 cm/s.

below the T_0 curve for the liquid composition at the interface. However, a criterion based on the diffusive speed of solute atoms seems to be a more useful sufficient condition at the present time.²¹ This criterion states that partitionless solidification should occur when the interface speed exceeds the speed at which solute atoms can diffuse away from the advancing interface. The diffusive speed is usually given as D/a where D is the liquid diffusion coefficient and a is the interatomic distance. For D typical of liquid metals ($2.5 \times 10^{-5} \text{ cm}^2/\text{s}$) and $a = 0.5$ nm, the diffusive speed is 500 cm/s. As shown in Figure 15, the initial growth rate is ~ 45 cm/s which is not high enough for significant nonequilibrium effects or solute trapping. Hence the microstructure of the zone solidified during recalescence is not microsegregation-free. For more dilute alloys or where k is not so small, higher solidification velocities can occur for identical initial undercooling and cell-free structures can be formed.

One might note that in powders which are smaller than 5 μm , the entire powder is microcellular. This suggests that for these small powders, $\Delta\theta' > 1$. With $L' = 0.7L$, $T_L - T_N > 250$ K and the calculated initial growth rate assuming local equilibrium would exceed 500 cm/s. However, at these rates the localized recalescence at the interface¹¹ would quickly reduce the growth rate to cause the major fraction of the powder particle to freeze at slower speeds. Furthermore, inclusion of the nonequilibrium partition coefficient would alter the predicted growth rate. The topic of solute trapping clearly requires further investigation as well as the factors which control the volume fraction solid within the microcellular zone during recalescence.

V. CONCLUSIONS

1. Rapidly solidified powders of Al-8 wt pct Fe exhibit four characteristic microstructures with increasing powder diameter between 5 and 45 μm : microcellular α -Al, cellular α -Al, α -Al + Al_6Fe eutectic, and Al_3Fe primary intermetallic structure.
2. Powders less than $\sim 10 \mu\text{m}$ in diameter undercool significantly prior to solidification typically yielding a two-zone microcellular-cellular structure across individual powder particles.
3. Larger particles do not exhibit a two-zone structure and exhibit cellular, eutectic, or primary intermetallic structures consistent with growth rates controlled only by heat extraction through the powder surface during solidification.
4. The presence of two-zone microstructures for initially undercooled powder particles, when the microstructure of both zones is cellular, is related to the dominance of solute redistribution on the growth rate.
5. Partitionless solidification of Al-8 wt pct Fe is not observed.

APPENDIX

Parameters for solidification of α -Al in Al-Fe alloys

m	= liquidus slope = -3.7 K/wt pct
k	= equilibrium partition coefficient = 0.038
$T_w\Gamma$	= capillary constant = $1 \times 10^{-5} \text{ Kcm}$
L	= latent heat of fusion = 971 J/cm^3
C	= liquid heat capacity = $2.67 \text{ J/cm}^3 \text{ K}$
L/C	= 364 K
D	= liquid diffusion coefficient = $2 \times 10^{-5} \text{ cm}^2/\text{s}$
α	= liquid thermal diffusivity = $0.34 \text{ cm}^2/\text{s}$
k_L	= liquid thermal conductivity = 0.92 J/cm s K
K_{gas}	= 75 pct of the thermal conductivity of argon at 0.1 MPa (1 atm) = $1.34 \times 10^{-4} \text{ J/cm s k}$

ACKNOWLEDGMENTS

This research was partially supported by the Naval Air Development Center, Warminster, PA. One of us (L. B.) would also like to thank the Defense Advanced Projects Agency for support. The authors would also like to ac-

knowledge the efforts of F. S. Biancanello, C. H. Brady, and D. Carrick. Discussions with J. H. Perepezko, University of Wisconsin-Madison; R. F. Sekerka, Carnegie-Mellon University; D. Shechtman, Technion; and S. R. Coriell, J. Murray, R. J. Schaefer, and P. W. Voorhees, National Bureau of Standards, were also very helpful.

REFERENCES

- 1 H. Jones *Mats Sci & Eng*, 1969 70, vol. 5, pp. 1-18
- 2 E. Blank *Z. Metallkunde*, 1972, vol. 63, pp. 315-23
- 3 P. Furrer and H. Warlimont *Z. Metallkunde*, 1973, vol. 64, pp. 236-48
- 4 M. H. Jacobs, A. G. Doggett, and M. J. Stowell *J. Mats Sci.*, 1974, vol. 9, pp. 1631-43
- 5 D. J. Skinner, K. Okazaki, and C. M. Adam in *Rapidly Solidified Powder Aluminum Alloys*, M. E. Fine and A. E. Starke, Jr., eds., ASTM-STP 890, Philadelphia, PA, 1986, pp. 211-36
- 6 J. L. Murray *Mat Res Soc Symp Proc.*, 1983, vol. 19, pp. 249-62
- 7 C. M. Adam and L. M. Hogan *J. Australian Inst. of Met.*, 1972, vol. 17, pp. 81-90
- 8 I. R. Hughes and H. Jones *J. Mats Sci.*, 1976, vol. 11, pp. 1781-93
- 9 J. H. Perepezko, S. E. LeBeau, B. A. Mueller, and G. J. Hildeman in *Rapidly Solidified Powder Aluminum Alloys*, M. E. Fine and A. E. Starke, Jr., eds., ASTM-STP 890, Philadelphia, PA, 1986, pp. 118-36
- 10 C. G. Levi and R. Mehrabian *Metall Trans. A*, 1982, vol. 13A, pp. 221-34
- 11 C. G. Levi and R. Mehrabian *Metall Trans. A*, 1982, vol. 13A, pp. 13-23
- 12 T. W. Clyne *Metall. Trans. B*, 1984, vol. 15B, pp. 369-81
- 13 D. Shechtman and E. Gutmanis *Prak. Metallografie*, 1981, vol. 18, pp. 587-93
- 14 C. M. Adam, in *Rapidly Solidified Amorphous and Crystalline Alloys*, B. H. Kear, B. C. Giessen, and M. Cohen, eds., Elsevier-North Holland, New York, NY, 1982, pp. 411-22
- 15 S. Dushman and J. Lafferty *Scientific Foundations of Vacuum Technique*, 2nd ed., John Wiley, New York, NY, 1962, p. 45
- 16 J. Lipton, M. E. Glicksman, and W. Kurz *Mats Sci. & Eng.*, 1984, vol. 65, pp. 57-63
- 17 W. J. Boettinger, S. R. Coriell, and R. F. Sekerka *Mats Sci. & Eng.*, 1984, vol. 65, pp. 27-36
- 18 J. H. Perepezko and J. S. Paik, in *Rapidly Solidified Amorphous and Crystalline Alloys*, B. H. Kear, B. C. Giessen, and M. Cohen, eds., Elsevier-North Holland, New York, NY, 1982, pp. 49-63
- 19 W. J. Boettinger and S. R. Coriell, NATO Advanced Research Workshop on *Rapid Solidification Technologies*, P. Sahn, ed., Amberg, FRG, 1985
- 20 M. Rappaz, Ph. Thevoz, and W. Kurz, in *Numerical Methods in Thermal Problems*, Part I, R. W. Lewis and K. Morgan, eds., Pine Ridge Press, Swansea, U.K., 1985, pp. 251-61
- 21 M. J. Aziz *J. Appl. Phys.*, 1982, vol. 53, pp. 1158-68

Rapidly solidified Al-Cr alloys: structure and decomposition behaviour

L. BENDERSKY

Center for Materials Research, The Johns Hopkins University, Baltimore, Maryland 21218 USA

R. J. SCHAEFER, F. S. BIANCANIELLO

Metallurgy Division, Center for Materials Science, National Bureau of Standards, Gaithersburg, Maryland 21771, USA

D. SHECHTMAN

Department of Materials Engineering, Technion, Haifa, Israel

Melt-spun ribbons of aluminium containing up to 15 wt% chromium were examined in the as-spun condition and after annealing. The more concentrated alloys contained multi-phase spherulites embedded in an α -Al matrix: chemical microanalysis showed the average composition of the spherulite core to be 22 ± 2 wt% chromium. The kinetics of precipitation at grain boundaries and within the matrix were determined by TEM and X-ray diffraction. Three very similar Al-Cr intermetallic phases are present under equilibrium conditions, but most of the precipitates in the melt-spun ribbons could be identified as Al₇Cr.

1. Introduction

Transition metals are commonly used as alloying elements to aluminium. Although they do not produce age hardening, they are added for various purposes, such as mechanical property improvement, recrystallization inhibition, stress corrosion prevention, etc. Due to the unfavourable electrochemical factor and the tendency of the components to form intermetallic phases, the range of solid solubility is extremely limited. It can, however, be significantly extended by rapid solidification [1-3]. The substantial increase in solid solubility offers the prospect of developing new alloy compositions with improved thermal stability. Several such additives as chromium, manganese and zirconium offer resistance to solute clustering during (or following) quenching [4, 5].

Rapidly solidified Al-Cr alloys exhibit a pronounced tendency to form metastable supersaturated solid solutions. This system has been investigated by several authors [5-15] who used different techniques of rapid quenching from the melt. Most previous studies [10-12, 14, 15] were limited to compositions of up to 3 wt% Cr, and some of them lack microstructural studies. Detailed electron microscopy investigation was performed by Warlimont *et al.* [8, 9] and Jones *et al.* [2, 5, 6]. Their studies were performed on compositions of up to 13 wt% Cr, and included study of the decomposition behaviour. These works are the main references for us.

In the present study we examined the microstructure of melt-spun ribbons which contain up to 15 wt% Cr. Thermal stability and decompositional behaviour were studied as a function of the chromium content and the temperature of isochronal heat treatment.

2. Experimental details

Alloy buttons with chromium concentrations of 1, 2, 5 and 15 wt% Cr were prepared by arc melting, using 99.999% Al and 99.95% Cr. For melt-spinning, small pieces cut from these buttons were induction heated in zirconia-coated quartz tubes. Immediately upon melting, the metal was squirted onto a copper melt-spinning wheel rotated at 6500 r.p.m. The process was carried out under helium at atmospheric pressure. The ribbons were typically 2 mm wide and 20 μ m thick. For annealing, the ribbons were sealed in borosilicate glass ampoules with a helium pressure of 1-2 atmosphere.

Lattice parameters were determined by measurements on an X-ray diffractometer, using filtered CuK α radiation. A Nelson-Riley procedure was used to obtain the lattice parameter from the measurements of the diffraction peaks. Simultaneous measurements of diffraction peaks from powdered high purity silicon were used as a normalization standard.

Three phases of apparently very similar crystal structure have been reported in aluminium rich Al-Cr alloys [16]: Al₇Cr or θ (21.6 wt% Cr), Al₁₁Cr₂ or η (25.96 wt% Cr) and Al₄Cr or ϵ (32.52 wt% Cr) are reported [9] to be very similar and no information on differences between them has been reported. We therefore prepared samples having the stoichiometric compositions of these compounds as X-ray diffraction references. These samples were first melt spun to reduce microsegregation, crushed and sieved to -325 mesh, and annealed at 600 °C for 16 h. X-ray diffraction patterns from these powders, using CuK α radiation, were then compared.

Microstructural studies were performed on a



Figure 1 As-spun ribbon of Al-2 wt% Cr alloy. A dislocation substructure is probably associated with slight microsegregation.

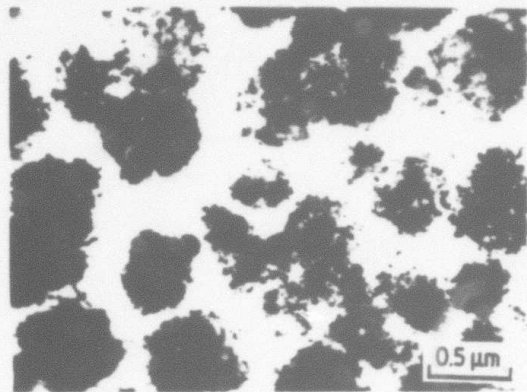


Figure 2 As-spun ribbon of Al-15 wt% Cr alloy. Spherulites embedded in aluminium matrix.

scanning transmission electron microscope. Chemical microanalysis was performed in the scanning transmission mode using a 5 nm probe. Quantification of the X-ray information was accomplished by using the Cliff-Lorimer method [17, 18], when the condition of the thin film approximation was maintained. X-ray intensity relates to composition by the expression $C_A/C_B = k_{AB} I_A/I_B$, where I_A and I_B are the measured characteristic X-ray intensities, and C_A and C_B are the weight fractions of two elements A and B (in our case aluminium and chromium). The coefficient $k_{Cr, Al}$ (constant in the thin film approximation) was found experimentally using the known phase θ -Al₇Cr as a standard: $k_{Al, Cr} = 0.91 \pm 0.1$.

The ribbons were thinned for STEM study by jet electropolishing in a standard solution.

3. Results

3.1. As-spun ribbons (TEM analysis)

The 1 and 2 wt% Cr alloys are one-phase supersaturated solid solutions of chromium in aluminium (maximum equilibrium solubility is 0.77 wt% Cr [18]). No second phase can be observed. A dislocation substructure is present and is probably associated with slight cellular microsegregation (see Fig. 1).

The 5 wt% Cr alloy has a transition microstructure between low and high concentration of chromium. In

some regions the microstructure consists of one-phase grains of supersaturated (5 wt% chromium) α -Al, with slight evidence of cellular structure and dislocation substructure (like the 1 and 2 wt% Cr alloys). In other regions the microstructure is characterized by multi-phase spherulites, embedded in α -Al matrix. Their volume fraction increases with increase of chromium concentration to reach homogeneous high density in the 15 wt% Cr alloy (see Fig. 2). The formation of spherulites was reported for the Al-Cr system by Furrer and Warlimont [9] and for several other systems by Shechtman and Horowitz [19].

The spherulites are generally composed of a core A (see Fig. 3a), surrounded by small petal-like crystals B measuring ~ 50 nm in size. The contrast of the petals is sometimes enhanced by Moiré fringes. The core has a two-phase structure, composed of very fine particles of size smaller than 5 nm. In some cases the spherulites are without petals on the periphery, as was found by Furrer and Warlimont [9]. Chemical microanalysis shows that the average composition of the core is 22 ± 2 wt% Cr. The composition of the matrix surrounding the spherulites is ~ 5 wt% Cr. A typical concentration profile of the microstructure is shown in Fig. 4, where gradual transition from 22 to 5 wt% Cr reflects a decrease in the density of petals embedded in the α -Al matrix. Dark field micrographs obtained with

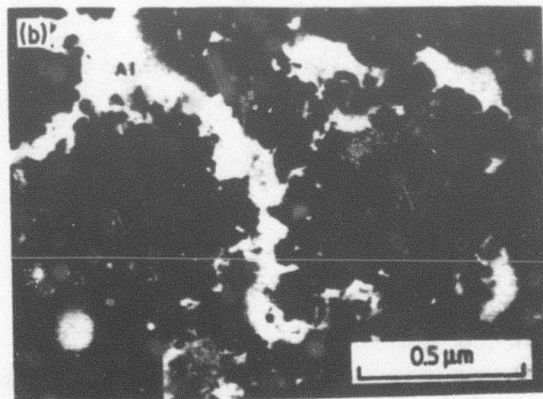
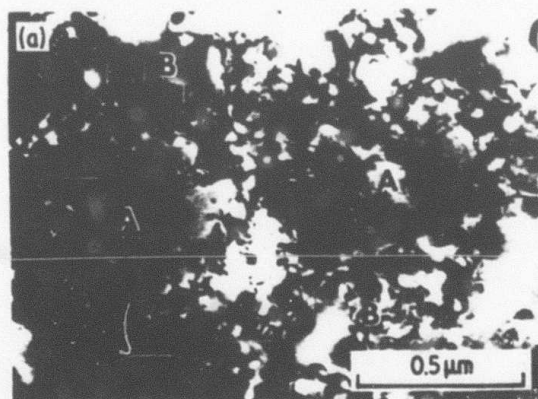


Figure 3 As-spun ribbon of Al-15 wt% Cr. (a) Bright field image of spherulites. The spherulites are composed of a core A, surrounded by petal-like crystals B (marked by arrow); (b) Dark field using an Al-matrix reflection. Surrounding matrix is α -Al.

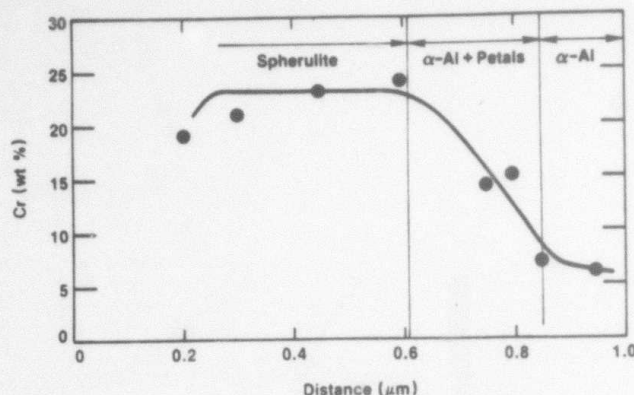


Figure 4 Composition profile across a spherulite.

an aluminium reflection (see Fig. 3b) confirms that the surrounding matrix is α -Al. A series of convergent beam diffraction patterns taken from different spherulites in the same matrix show that the spherulites are randomly oriented. These diffraction patterns are a combination of two or more single patterns of intermetallics with orientational coherence between them. No aluminium reflections were found here. This contradicts some results obtained by Furrer and Warlimont [9] who concluded that spherulites are composed of randomly oriented precipitates within the aluminium matrix.

Analysis of convergent beam diffraction patterns from the petals shows that they have the structure of the θ -Al₇Cr phase (see Fig. 5), which is monoclinic with $a = 2.531$ nm; $b = 0.754$ nm; $c = 1.0949$ nm; $\beta = 128^\circ 71'$ [20]. Dark field micrographs (Fig. 6) obtained with an intermetallic reflection show the possibility that the petals and at least one group of fine precipitates in the core have the same structure.

3.2. Heat treated ribbons (TEM analysis)

The decomposition behaviour of the alloys was studied in the range of temperatures 250 to 550°C for composition of 1, 2 and 5 wt % Cr. For most cases the

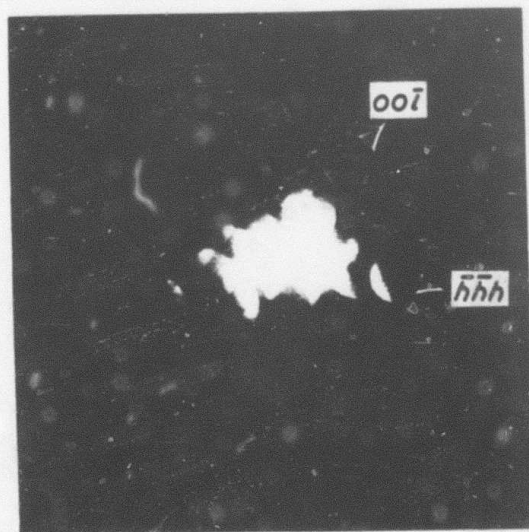


Figure 5 Microdiffraction from the "petal" [110] zone axis of Al₇Cr. Arrows show directions (00l) and (hhh) of reflection rows.

annealing time was 6 h, however for some up to 100 h. Generally, supersaturated aluminium decomposes at the grain boundaries and within grains to form needle- or plate-like precipitates of the equilibrium phase θ -Al₇Cr, with no indication of any transition phase, in agreement with others [5, 6, 15].

Analysis of samples annealed for 6 h shows that grain boundary precipitation (GBP) starts at a lower temperature than matrix precipitation (MP). The difference is roughly 50°C. The temperature at which decomposition starts (where the second phase is first observed) depends strongly on the degree of supersaturation. Fig. 7 shows the summarized results, where the curves represent the beginning of the GBP and MP decomposition. Annealing up to 100 h at temperatures of GBP start results in the appearance of only GB precipitates, without any matrix precipitation (see Fig. 8). At temperatures above the MP start curve, fast growth of matrix precipitates occurs, until the supersaturated matrix is completely relaxed (see Fig. 9). Selected area electron diffraction indicates that both grain boundary and matrix precipitates are θ -Al₇Cr (Fig. 10). It was found the longest axis of the precipitates is parallel to the $\langle 011 \rangle_{Al}$ direction.

The microstructure after annealing at temperatures below the curve of GBP start (Fig. 7) is characterized by finely dispersed strain contrast (see Fig. 11). No distortion of diffraction spots or super-lattice reflections were found. Annealing at higher temperatures or for longer time does not change the character of diffraction, but the contrast appears to be more intensive (Fig. 12) and the centres of strain contrast are less dense. In certain cases it is possible to resolve it as loops (Fig. 13). These loops or clusters have very high thermal stability and exist up to 500°C (see Fig. 14).

3.3. X-ray studies

The measured lattice parameters of the as-spun 1, 2 and 5 wt % Cr ribbons are within 10^{-4} nm of the values collected by Midson *et al.* [5] for rapidly solidified alloys (Fig. 15). No indication of phases other than aluminium is seen in the X-ray diffraction patterns of these alloys. Upon annealing for 6 h, no significant change of lattice parameter is seen at temperatures of 400°C or less. At 450°C the lattice parameter of the 5 wt % Cr alloy has started to shift, and at 500°C the supersaturation of the 5% and 2% alloys has mostly disappeared (Fig. 15).

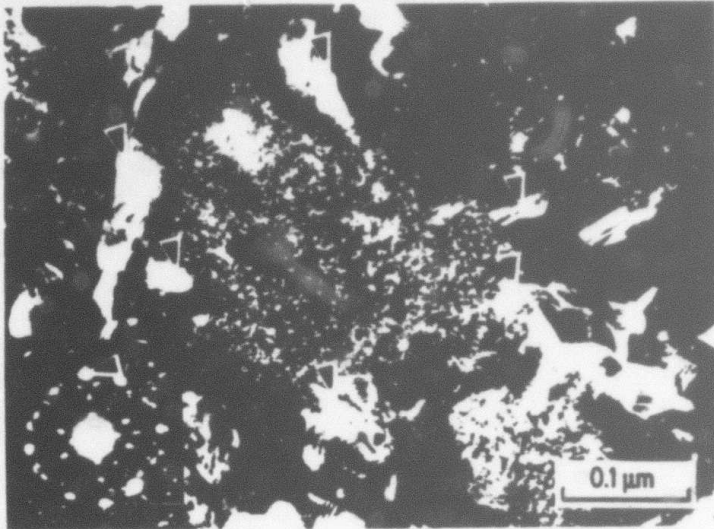


Figure 6 Dark field using an intermetallic reflection. Fine precipitates in spherulite core and some petals (marked by arrows) reflect at the same time.

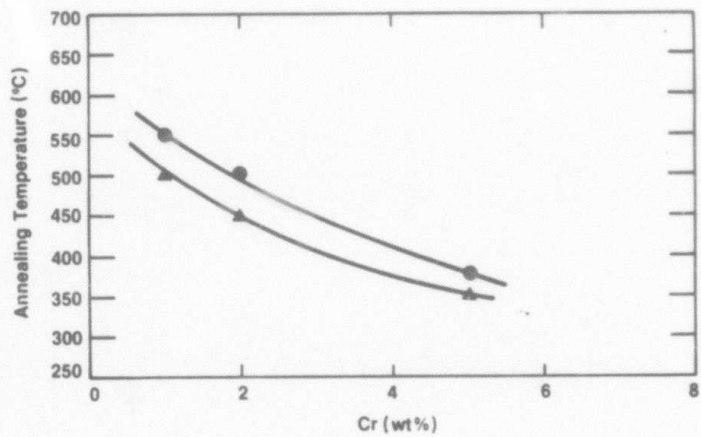


Figure 7 Annealing temperature-composition diagram, where curves represent the beginning of precipitation (▲) on grain boundaries (GBP) and (●) inside the grains (MP) for 6 h anneals.



Figure 8 The Al-2 wt% Cr following 100 h at 400° C containing Al, Cr particles mostly along grain boundaries.

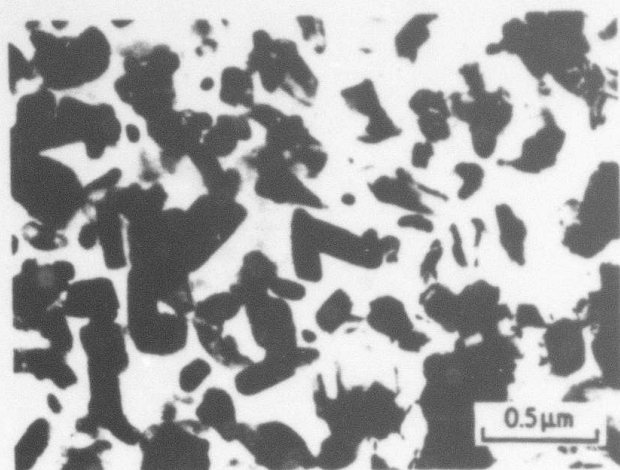


Figure 9 The Al-5wt% Cr following 6 h at 550°C containing Al₃Cr particles within the grains.

X-ray diffraction peaks from intermetallic phases are first seen after 6 h at temperatures as low as 400°C (Fig. 16) and become progressively stronger at higher temperatures. Analysis of alloys having stoichiometric compositions shows that only the θ -Al₃Cr sample had a peak at $2\theta = 21.7^\circ$, only the ϵ -Al₄Cr sample had peaks at $2\theta = 17^\circ$ and 26.6° , and the η -Al₁₁Cr₂ sample showed none of these peaks. In addition, there was a substantial difference in the detailed distribution of intense peaks in the region between $2\theta = 36$ – 46° , with the pattern from the θ -Al₃Cr sample corresponding well to a pattern computed from structural data reported for this phase [20] as shown in Fig. 16. It should be noted that the diffraction patterns of these samples were significantly different in the as-solidified condition and after annealing at 600°C, as would be expected from the phase diagram.

On the basis of the diffraction patterns of the reference samples, the precipitates in the annealed ribbons are identified as shown in Fig. 17. In the earlier stages of precipitation, however, the phase identification can only be tentative.

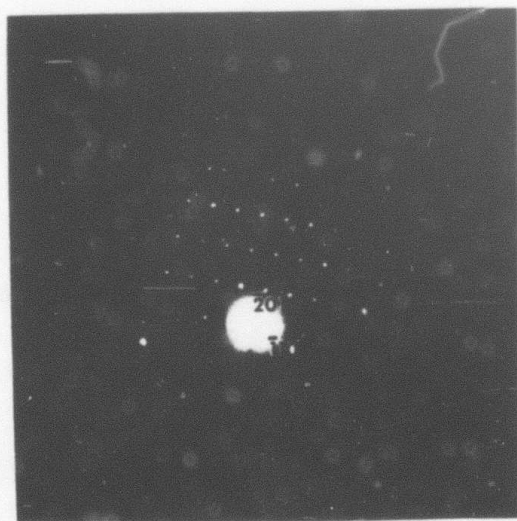


Figure 10 Diffraction pattern typical for both grain boundary and matrix precipitates. [112] axis zone of Al₃Cr.

The diffraction pattern of the as-spun 15 wt% Cr alloy shows peaks corresponding to the icosahedral phase [21] as well as peaks which could be attributed to any of the equilibrium phases θ , η or ϵ . After annealing for 6 h at 350°C or higher, intermetallic peaks clearly corresponding to θ -Al₃Cr are observed. An as-spun ribbon containing 20 wt% Cr showed diffraction peaks only from α -Al and the icosahedral phase, with none from θ , η or ϵ .

4. Discussion

Highly extended solid solubility can be achieved for melt-spun ribbons of Al-Cr. In our experiments the extension is up to 5 wt% Cr, and we believe that it is close to the maximum one can get by this technique of melt quenching. The maximum was established to be 7 wt% Cr for two-piston [5] and splat [9] quenching for a thickness of $\sim 50 \mu\text{m}$. Higher values up to 10 wt% Cr were attainable for very thin sections, e.g. of gun splats [8, 9, 22]. These differences in solid solubility maximum reflect the sensitivity to the changes in cooling rate in the range 10^6 to 10^8 K sec^{-1} and to the degree of supercooling, accordingly [7].

Aluminum containing small concentrations of chromium is expected to solidify without microsegregation at relatively low velocities on the basis of the absolute stability effect of morphological stability theory [23]. Because the solute partition coefficient in this system is relatively close to unity (although not known with precision), the absolute stability effect is predicted to occur at relatively low velocities (or high concentrations) compared to a system such as Al-Fe [19], where the solute partition coefficient is extremely small. This effect accounts for the absence or rarity of cellular substructures in the alloys containing 1, 2 or 5 wt% Cr.

At higher concentration ($> 5 \text{ wt}\%$ Cr) the competitive solidification of intermetallic phases begins. They appear within the liquid and grow as spherulites to $\sim 1 \mu\text{m}$ diameter before being engulfed by the solidifying supersaturated aluminum front. The spherulite volume density increases with increasing chromium concentration. For the 15 wt% Cr alloy the solidification of spherulites is the dominant mode. The appearance of spherulites influences the mechanical

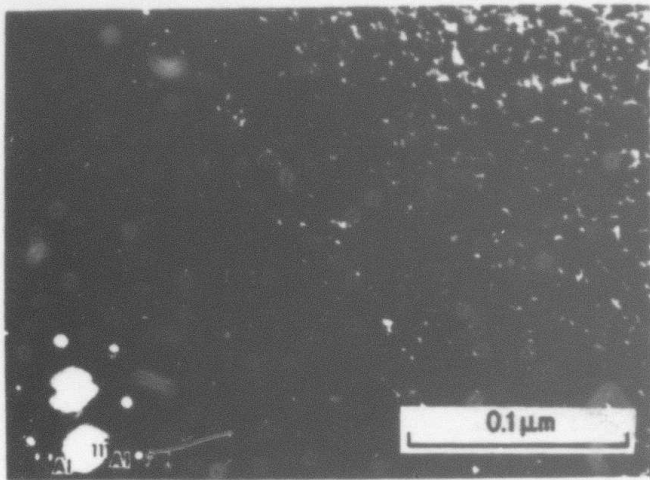


Figure 11 The Al-5 wt% Cr following 100 h at 300° C. Dark field using (111) reflection of aluminium. Fringe strain contrast. Diffraction pattern is entirely of α -Al.

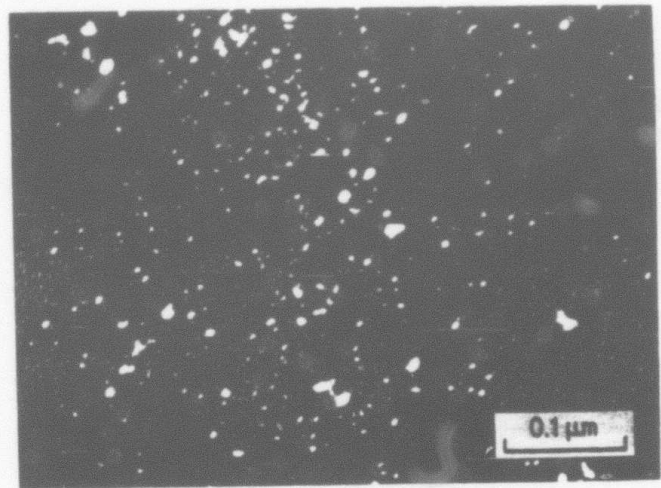


Figure 12 The Al-1 wt Cr following 6 h at 500° C. Dark field using (111) reflection of aluminium at weak beam condition. Strain contrast is enhanced compared to Fig. 13. Diffraction pattern is entirely of α -Al.

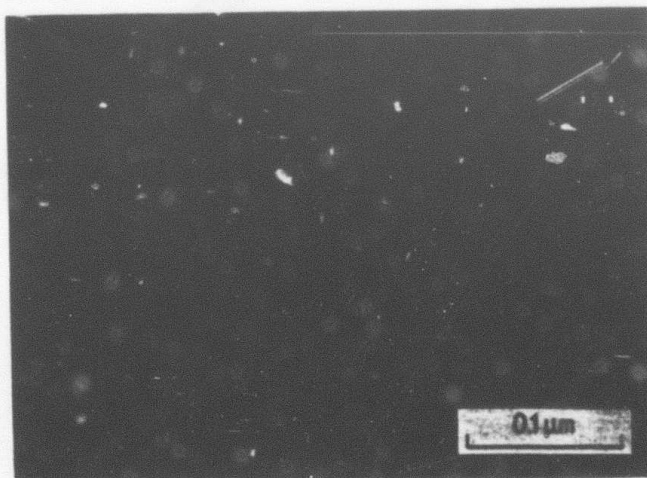


Figure 13 The Al-1 wt% Cr following 6 h at 450° C. Dark field using (020) reflection of aluminium at weak beam condition of dislocations loops.

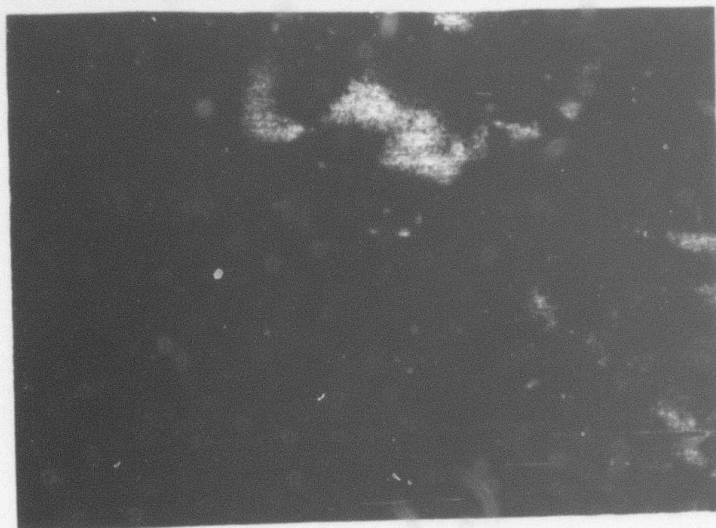


Figure 14 The Al-2 wt % Cr following 6 h at 500° C. Bright field micrograph shows coexistence of Al,Cr precipitates and objects of strain contrast.

properties. For example, Yakunin *et al.* [24] reported decreasing tensile strength for alloys with compositions higher than 8 wt % Cr. Solidification as separated spherulites is an unusual pattern in rapid solidification, although common in concentrated aluminium-transition metal alloys, e.g. in Al-Fe (> 11 wt % Fe) and Al-Mn (> 15 wt % Mn) [19, 25]. The increase of spherulite volume density points out that the nucleation rate for the intermetallic phase starts to be dominant compared to the nucleation rate for α -Al as the concentration of the alloy increases. The steep increase of the intermetallic liquidus with concentration, compared to the slow change for the α -Al liquidus, provides different rates of change in supercooling with concentration. The supercooling as a function of chromium content changes very little for α -Al, while it strongly increases for the intermetallic. Accordingly, the relative nucleation rate depends on the concentration.

Equilibrium freezing concepts would predict that in the 5 wt % Cr alloy the η -Al₁₁Cr₂ phase would form

first from the liquid and the θ -Al₇Cr phase would then form by a peritectic reaction, whereas in the 15 wt % Cr alloy, primary ϵ -Al₄Mn phase would form, followed by peritectic η and θ . Under rapid solidification conditions, however, the equilibrium phases may be suppressed. The core of the spherulites formed in the 15 wt % Cr alloy, which has a composition midway between that of the θ and η phases, could thus have initially solidified from the melt as any of the intermetallic phases and subsequently decomposed in the solid state during cooling of the ribbon into a mixture of θ and η .

It should be noted that the equilibrium boundaries of the θ , η and ϵ phases are not well established, and the θ and η phases are reported to be structurally identical [26]. The exact identification of the many very fine crystallites which appear in the rapidly solidified materials is therefore difficult, and even the prediction of the relative stability of the different phases is questionable.

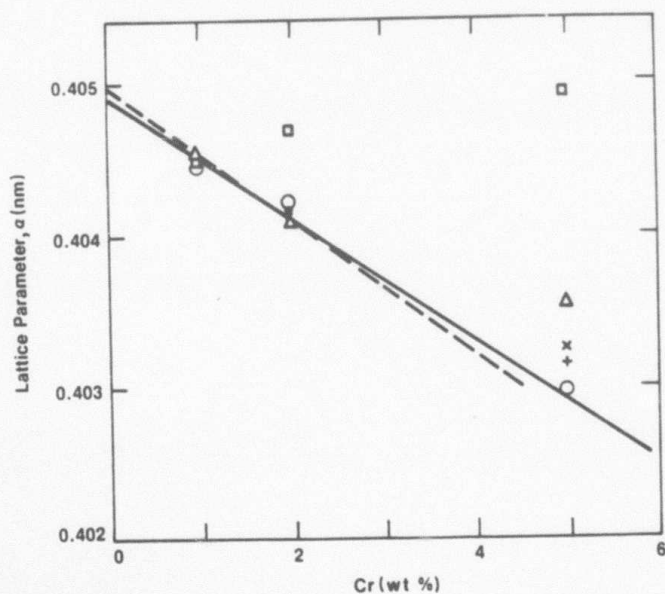


Figure 15 Lattice parameter of Al-Cr alloys, compared to data previously reported in (—) [3] and (---) [12]. (S+) as-spun. 6 h anneals at the following temperatures (○) 350° C, (×) 400° C, (Δ) 450° C, (□) 500° C.

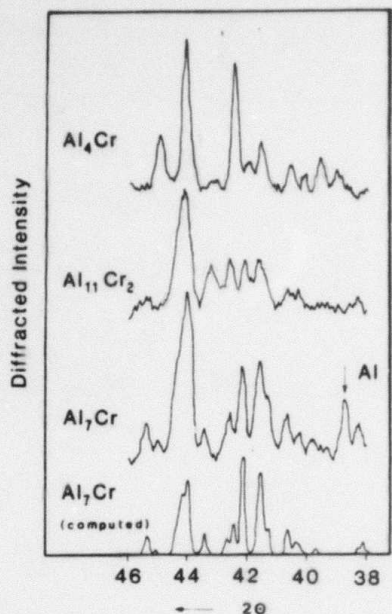


Figure 16 Diffraction patterns of CuK α radiation from samples having the stoichiometric compositions of the Al-Cr intermetallic compounds. Samples were melt spun, crushed, and annealed at 600°C for 16 h.

5. Conclusions

1. By melt-spinning, the concentration of chromium in solid solution in aluminium can be extended to approximately 5 wt %. As the chromium concentration is increased beyond 5 wt %, increasing numbers of chromium-rich spherulites are formed during solidification.

2. The spherulites have a core, consisting of very fine grains of two or more intermetallic phases, surrounded by petal-like crystals of the θ -Al₇Cr phase. The average composition of the core is 22 ± 2 wt % Cr.

3. Precipitation at grain boundaries occurs at temperatures lower than those which produce precipitation in the matrix. These temperatures are strongly dependent upon the sample composition.

Acknowledgement

The authors thank DARPA for financial support of this work.

References

- H. JONES, *Aluminium* **54** (1978) 274.
- S. P. MIDSON and H. JONES, in Proceedings of 4th

International Conference on Rapid Quenched Metals, Sendai, 1981 (Japan Institute of Metals) p. 1539.

- G. FALKENHAGEN and W. HOFMANN, *Zh. Metall.* **43** (1952) 69.
- H. JONES, "Vacancies '76" edited by R. E. Smallman and J. E. Morris (The Metals Society, London, 1977) p. 175.
- S. P. MIDSON, R. A. BUCKLEY and H. JONES, Proceedings 4th Conference on Rapidly Quenched Metals, Sendai, 1981 (Japan Institute of Metals) p. 1521.
- H. JONES, "Rapid Solidification Processing, Principles and Technology II," edited by R. Mehrabian, B. Kear and M. Cohen (Claitor's, Baton Rouge, 1980) p. 306.
- R. ICHIKAWA, T. OHASHI and T. IKEDA, *Trans. Jpn. Inst. Metals* **12** (1971) 280.
- H. WARLIMONT, W. ZINGG and P. FURRER, *Mater. Sci. Eng.* **23** (1976) 101.
- P. FURRER and H. WARLIMONT, *ibid.* **28** (1977) 127.
- N. I. VARICH and R. B. ZYUKEVICH, *Russian Metall.* **4** (1970) 58.
- Idem*, *Izv. Acad. Nauk. Met.* **4** (1970) 82.
- A. F. POLESYA and A. I. STEPINA, *Fiz. Met. Metall.* **27** (1969) 885.
- R. D. VENGRENOVICH and V. I. PSAREV, *ibid.* **29** (1970) 540.
- V. I. DOBATKIN, V. I. ELAGIN, V. M. FEDOROV and R. M. SIZOV, *Izv. Acad. Nauk, Metall.* **2** (1970) 199.
- K. NAGAHAMA and I. MIKI, *Trans. Jpn. Inst. Metals* **15** (1974) 185.
- A. J. BRADLEY and S. S. LU, *J. Inst. Metals* **60** (1937) 319.
- G. CLIFF and G. W. LORIMER, *J. Microsc.* **62** (1975) 246.
- N. J. ZALUZEC, "Introduction to Analytical Electron Microscopy," edited by J. J. Hren, J. I. Goldstein and D. C. Joy (Plenum, 1979) p. 121.
- D. SHECHTMAN and E. HOROWITZ, "Metastable Phases of Rapidly Solidified Al-Rich Al-Fe Alloys," Quarterly Reported DARPA Order No. MDA-903-83-K-0400, January (1984).
- M. J. COOPER, *Acta Cryst.* **13**(1960) 257.
- D. SHECHTMAN, I. BLECH, D. GRATIAS and J. W. CAHN, *Phys. Rev. Lett.* **53** (1984) 1951.
- L. M. BUROV and A. A. YAKUNIN, *Russ. J. Phys. Chem.* **42** (1968) 540.
- S. R. CORIELL, R. F. SEKERKA, *J. Crystal Growth* **61** (1983) 499.
- A. A. YAKUNIN, L. F. SILKA and A. B. LISENKO, *Fiz. Met. Metall.* **56** (1983) 945.
- D. SHECHTMAN, private communication (1984).
- R. P. ELLIOTT, "Constitution of Binary Alloys, First Supplement," (McGraw-Hill, New York, 1965) p. 33.

Received 5 November 1984

and accepted 11 July 1985

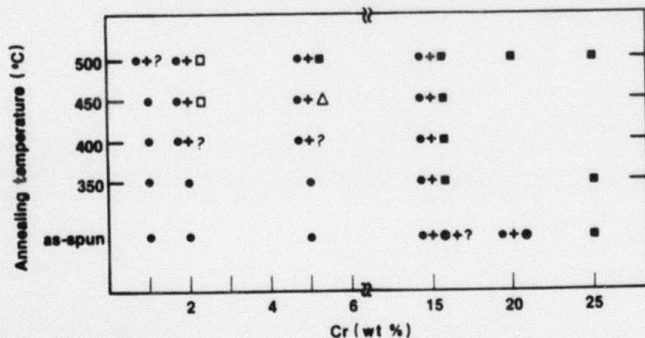


Figure 17 Phases observed by X-ray diffraction in melt-spun and annealed Al-Cr ribbons. 6 h anneals. (●) Aluminium, (■) Al₇Cr, (□) tentative, (▲) Al₁₁Cr₂, (△) tentative, (⊗) icosahedral phase, (?) indistinguishable, Al-Cr, Al₁₁Cr₂, or Al₄Cr.